RESEARCH

Estimation of photo-degradation of dielectrics surrounding the narrow channel due to PD activity

Alireza A. Ganjovi

Abstract Partial discharge (PD) taking place within narrow channels produces a large number of charged particles, causing degradation of the polymer. Additionally, PD pulses also produce UV photons due to decay of excited states (radiative states) in air. These may have enough energy to break C–C bonds and thereby add to the degradation of the dielectrics surrounding the narrow channel. In this paper, a radiation transport (RT) model has been developed and integrated with a Particle-in-Cell/ Monte Carlo collision (PIC-MCC) model to study the behavior of excited (radiative) states of air within discharge in the narrow channel. The radiative state atoms are described by a fluid model combined with the Holstein–Biberman equation. This model has the ablation to follow the spatial evolution of the radiative excited-state density throughout narrow channel. The effect of applied electric field, narrow channel dimensions, gas pressure on the extent of degradation of dielectrics surrounding the narrow channel is studied.

Keywords Spark-type partial discharge · Dielectric degradation · Radiation transport model · PIC-MCC simulation

Introduction

Partial discharge (PD) pulses occurring within the narrow channels are responsible for causing degradation of the surrounding dielectric material. Degradation is defined as a process which leads to a deterioration of any physical property of a polymer [1, 2]. Degradation of the narrow channel walls is a complex process, and some of principal mechanisms involved are mechanical erosion, thermal and chemical decomposition of the polymeric material.

Observation of light emission during PD activity in fact has been well established and reported by many authors [3–15]. Light emission during electrical discharges in the narrow channels gives us information about spatial distribution of PD.

Laurent et al. [3, 4] investigated the growth of electrical trees through the simultaneous measurement of light intensity and PD. A photomultiplier tube (PMT) was used to detect light emission at the tip of a needle electrode embedded in LDPE. They studied radiation emission in insulating materials (LDPE) used for cables. Further, they [5] evaluated the gases appearing in the channels of bush and branch-like electrical trees in LDPE and cross-linked polyethylene (XLPE) when subjected to a strong alternating electric field. They report that the emission spectra obtained confirm the presence of hydrogen and carbon oxides.

A quantitative study was done by Champion et al. [6] on light emission during initiation and the early growth stages of electrical treeing in synthetic resins. The three types of light emission observed by them are as follows: (a) electroluminescence caused by charge injection based on Fowler–Nordheim or Schottky effect dependent on local electric field, (b) micro-discharge activity along with formation of narrow channels and (c) conventional PD

A. A. Ganjovi (✉)
Photonics Research Institute, Institute of Science and High Technology and Environmental Sciences, Graduate University of Advanced Technology, Kerman, Iran
e-mail: alirezaganjovi@yahoo.com; ganjovi@icst.ac.ir; ganjovi@kgut.ac.ir

activity within narrow channel. Champion et al. [7] found that under long-term continuous electrical stress, light emission is found to spread principally along the cone of the pin rather than into the resin. In another work [8, 9], they observed the spatial distributions of light emission in various types of trees (bush, bush/branch, branch).

Kaneiwa et al. [10] attempted to understand the mechanism of degradation through electrical treeing and tree propagation using an artificial tree channel in LDPE, from which tree propagation occurred. It was seen that the region of light emission reaches the vicinity of the channel tip before tree propagation. In those samples where tree did not propagate, the region of light emission due to PD does not reach the channel tip. They concluded that tree propagation occurs only when large magnitude PDs are present; long luminous regions occur within the artificial channel and damage the channel tip before tree initiation. Kaneiwa et al. [11] further observed that for positive PD, the light emission is near the needle-tip and a positive correlation is to be found between the PD magnitude and the length of luminous region. They concluded that PD starts at the needle tip and the PD magnitude is determined by the PD length. For negative PD, there appeared to be no correlation between the PD magnitude and the length of luminous region.

Wu et al. [12–15] reported that in a long-narrow channel, the behavior of PD is similar to that in an actual tree and the range of light emission in the channel increases when the applied voltage increases.

The main source of light emission within air-filled narrow channels during PD activity is emission from the second positive system (2P) of N_2 ($C^3\Pi_u \rightarrow B^3\Pi_g$) [16]. They are UV photons in the range of 300 (4.13 eV) to 406 nm (3.05 eV). As mentioned earlier, the UV light produced inside the channel is due to the decay of excited states and can cause photo-degradation of the surfaces surrounding the narrow channel. It would be expected that the predominant products of radiolysis of linear alkanes would be due to the rupture of C–C bonds [17–19]. This process would be particularly sensitive to electric fields if charged species such as radical ions are formed as intermediates, or if they bring about changes in the dielectric constant by altering the concentrations of polar species [17–19].

It is obvious that light emission plays an important role in PD pulses. As far as we are aware, there is no theoretical model to simulate generation and propagation of photons within narrow channels, and their subsequent effect on the surrounding dielectrics.

In previous works [20], a two-dimensional Particle in Cell-Monte Carlo Collision (PIC-MCC) model [21–23] to study the effect of similarities and dissimilarities of electrodes on the spark-type PD pulses in sub-millimeter sized

cavities was developed. Moreover, the effect of applied electric field on the damage due to partial discharges activity into the surroundings dielectrics of a narrow channel encapsulated within the volume of a dielectric material was evaluated using this model [24]. Based on this model, the effects of different parameters of PD activity in the narrow channel on the damage into the surroundings dielectrics were studied [25]. In this paper, the above PIC-MCC model coupled with a Radiation Transport (RT) model [26–39] is used to describe the production of UV radiation inside narrow channel and its interaction with surrounding dielectrics. This RT-PIC model incorporates the resonance trapping effect of photons, to the kinetic model of the charged particles when a PD pulse develops inside a narrow channel. This model allows us to follow the spatial evolution of the density of radiative excited state (photons) within the narrow channel. The effect of applied electric field and micro-channel length on the extent of degradation of dielectric anode, cathode and side-walls, based on C–C bonds breaking due to UV photons impact, is studied.

Simulation model

Computational method for PD within narrow channel

In the PIC scheme, particles are defined in a continuum position and velocity space. Field values are defined at discrete locations in space. Particle and field values are advanced sequentially in time, starting from initial conditions. The particle equations of motion are solved at every time step, using field values interpolated from the discrete grid to particle locations. The force on every particle is computed by interpolation of the field values from the grid position to the given particle positions. The position and velocities of each particle is next updated based on the solution of the classical equation of motion [40]. Next, particle boundary conditions are applied. For modeling collisions, the Monte Carlo collision (MCC) scheme is applied [41]. Source terms for the field equations are accumulated from the particle locations to the grid locations. The field values are then advanced by one time-step, and the time loop starts again (Fig. 1).

In the PIC-MCC scheme, each super-particle, representative of one or a much larger number of real particles, is designated in continuum space by its position and velocity. Initially, a Maxwellian distribution is assumed for electrons and ions. Further, the particles are uniformly distributed in the gap space. Particle boundary conditions such as absorption and emission are used to account for the relation between the discharge current in the gap and the current in the external circuit. When an electron or ion
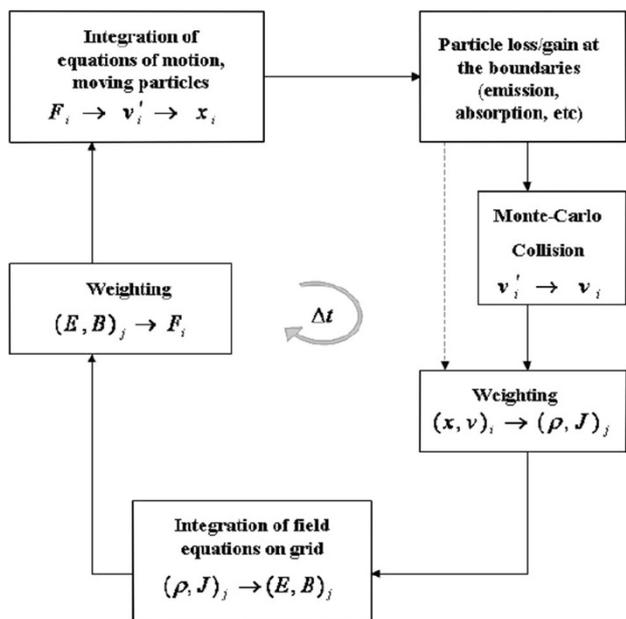
Fig. 1 Schematic representation of the computation sequence for Particle in Cell-Monte Carlo (PIC-MCC) method

passes from the discharge into an end wall, it adds to the wall charge and is deleted from the list of active particles [23]. Additionally, secondary emissions occur when a charged particle impacts a surface (metallic or dielectric) causing ejection of electrons from the surface.

In the current work, the gas within the cavity is assumed to be air at atmospheric pressure. Therefore, photo-emission at the cathode is likely to be the dominant secondary emission process, rather than electron emission from cathode or anode due to ion or electron bombardment. However, all of the above processes have been accounted for in the model. After emission of a new electron, its energy is also assigned from an assumed Maxwell–Boltzmann distribution. The interaction of charged particles with neutral atoms and molecules, and other collisional processes are included by using a Monte Carlo Collision technique [42]. Three main charged particle species, viz. electrons, positive ions and negative ions have been considered. The major electron-neutral molecule impact reactions included are (i) elastic, (ii) excitation, (iii) ionization (including all important ionization reactions) and (iv) electron attachment. Related cross-sectional values are extracted from experimental data available in the literature [29]. Integral cross-section values for electron interaction in dry air have been determined from its molecular constituents by assuming a target composition of 78.09 % N_2 and 21.19 % O_2 [43]. Only elastic and charge transfer collisions between ions and neutrals are considered. Because ion–molecule cross-sections are not readily available, a constant cross-section (10^{-20} m^2) has been assumed based on a hard-sphere collision model [44].

A significant contribution of this work is that the discharge within the cavity is simulated in conjunction with an external circuit comprising of a voltage source, and a blocking capacitor that stops the flow of any average current. The coupling between the charge flow within the micro-cavity and the external current is obtained via the parallel-plane electrodes, which may be metallic or dielectric, depending on the location of the discharge site.

The potentials and fields are obtained using Poisson's equation:

$$\nabla \cdot \varepsilon_0 \nabla \Phi(x,t) = \rho(x,t) \tag{1}$$

The potential (Φ) can be separated as follows [42, 45, 46]:

$$\Phi = \Phi_P + \sum_{\text{Boundaries}} \Phi_L \tag{2}$$

where Φ_P and Φ_L represent the Poisson and Laplacian parts of electrical potential (Φ).

Therefore, the field may be described by the combination of the following equations:

$$\nabla \cdot \varepsilon_0 \nabla \Phi_P = -\rho \tag{3}$$

$$\nabla \cdot \varepsilon_0 \nabla \Phi_{Li} = 0 \tag{4}$$

The boundary condition for Eq. (3) is $\Phi = 0$ on all boundaries as the Poisson field is solely due to charge in the medium. For each boundary with a Dirichlet condition, Eq. (4) is solved for $\Phi_i = 0$ on the equipotential surface, and $\Phi = 0$ elsewhere which gives us Φ_{Li} (the potential due to the ith Laplacian field). Φ_L is obtained by the superposition of all the Laplacian fields. Neumann boundary conditions are included through $\Phi_P = 0$. This method neglects charges induced by a driven electrode on other boundaries which are connected to an external circuit. It is also possible to solve the field Poisson equation with boundaries and circuits [40, 42, 47].

In this work, identical cavities, as might occur at discharge sites, with two different electrode configurations have thus been considered. These are the two generic cases described below. The model is two-dimensional with Neumann boundary conditions on the side-walls. Dirichlet boundary conditions (potential drop specified) are assumed on the electrodes.

A narrow channel bounded by dielectrics on both sides is depicted in Fig. 2a. The equivalent circuit of this configuration is shown in Fig. 2b, where C_g, C_{d1}, C_{d2} and C_r represent the equivalent capacitances of the gap, the dielectric layers and dielectric material parallel to the micro-channel, respectively. The discharge current may be represented by I_{conv}. Using KCL, it is possible to obtain the following relations [21]:

$$C_d \frac{dU_d}{dt} = I_{\text{ext}} - I_r \tag{5}$$

(a)

(b)
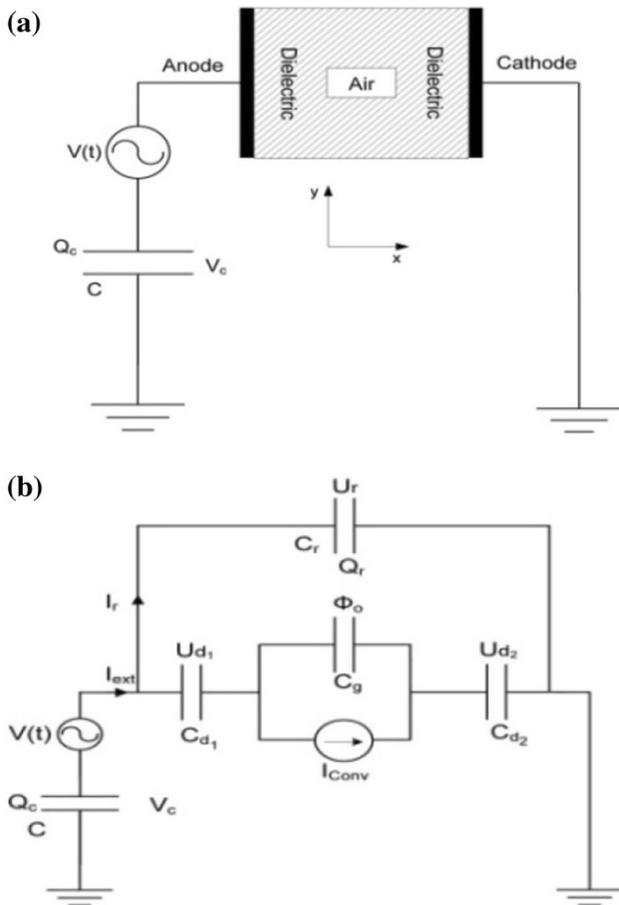
Fig. 2 **a** The geometry of two dimensional dielectric–dielectric narrow channel; the external circuit consists of a voltage source and a blocking capacitor which stops the flow of average current, **b** the corresponding equivalent circuit

$$A\frac{\mathrm{d}\sigma_s}{\mathrm{d}t} = I_{\text{ext}} - I_{\text{r}} + AJ_{\text{conv}} \tag{6}$$

$$V_c = V(t) - 2U_d - \varphi_0 \tag{7}$$

$$U_{\text{r}} = 2U_d + \varphi_0 \tag{8}$$

where I_{ext} and σ_{T} are the total external current and charge on the dielectric surface. I_{r} is the leakage current flowing in the bulk of dielectric material parallel to the narrow channel. By combining the above equations, Equation (27) in ref. [21] may be rewritten as follows:

$$\varphi_0^t = \left(\sigma_{s_{\text{T}}}^{t-1} + \frac{1}{A}(\alpha CV(t) - \alpha Q_c^{t-1} + \alpha Q_{\text{r}}^{t-1} \right.$$
$$\left. - 2\alpha(C + C_{\text{r}})U_d^{t-1} + Q_{\text{Conv}}^t) + \frac{\Delta x}{2}\sum_{j=0}^{j=N}\rho_{0j} \right.$$
$$\left. + \frac{\varepsilon}{\Delta x}\sum_{j=0}^{j=N}\varphi_{1j}^t \right)\left(\frac{\varepsilon}{\Delta x}N + \alpha(C + C_{\text{r}})/A \right)^{-1} \tag{9}$$

where $\alpha = (1 + 2(C + C_{\text{r}})/C_d)^{-1}$. σ_{T}, A, C, $V(t)$, Q_c, Q_{r}, Q_{conv}, ρ, φ_{ij} and N_j are respectively the total surface charge density on the electrodes at a given time 't', cross-sectional area of electrode, capacitance of blocking capacitor, driving voltage, charge in the external circuit, charge in the bulk of dielectric material parallel to the narrow channel, charge convection due to discharge, space charge density, the electric potential at each grid point and the number of grid divisions along the y-axis. The derivation of Eq. (9) is presented in "Appendix 1".

Model for radiation transport

The PIC-MCC model for gas discharge within narrow channel is described in detail in ref. [20, 24, 25]. In this section, we describe the radiation transport model for photons dynamics.

For both N_2 and air, the excitation coefficient is assumed to be that representing the second positive system of N_2 [48]. Hence, in this study, we consider the radiation trapping of the photons emitted from the second positive system (2P) of $N_2(C^3\Pi_u \rightarrow B^3\Pi_g)$ [48, 49]. The radiation transport equation is included with the PFM [34] and the neutral gas density profile is assumed to be uniform, which is valid for the pressure regime concerned. Because the cell is operated at atmospheric pressure, broadening with a Lorentz line shape is dominant. It has been assumed that the frequency of a re-emitted photon is completely independent of that of the absorbed photon.

The modified Holstein equation for the resonant (radiative) state density is as follows [39]:

$$\frac{\partial n^{\text{r}}(r,t)}{\partial t} = P_{\text{r}}(r,t) - \frac{1}{\tau_v}n^{\text{r}}(r,t)$$
$$+ \nabla.D_{\text{r}}\nabla n^{\text{r}}(r,t) + \frac{1}{\tau_v}\int n^{\text{r}}(r',t)G(r,r')\mathrm{d}r', \tag{10}$$

where $n^r(r,t)$ and $P_r(r,t)$ are the radiative excited state density and their production rate inside the micro-channel. τ_v is the vacuum radiative decay time, which is around 40 ns for air ($N_2(C^3\Pi_u \rightarrow B^3\Pi_g)$) [40], $G(r, \acute{r})$ is the kernel function, which is the probability for a resonance photon emitted at the position $\acute{r}$ to be absorbed at position r. The calculation of $G(r, \acute{r})$ is presented in ref. [39].

The total radiation flux at the dielectric anode and cathode surface is:

$$F^{\text{anode}}(y_i) = \sum_{j=1}^{N_x}\sum_{k=1}^{N_y}n_{jk}^{\text{r}}F_{|i-j|,k}^{\text{anode}} \tag{11}$$

$$F^{\text{cathode}}(y_i) = \sum_{j=1}^{N_x}\sum_{k=1}^{N_y}n_{jk}^{r}F_{|i-j|,k}^{\text{cathode}} \tag{12}$$

and at dielectric side-walls:

$$F^{\text{side-walls}}(x_i) = \sum_{j=1}^{N_x} \sum_{k=1}^{N_y} n_{jk}^r F_{|i-j|,k}^{\text{side-walls}} \qquad (13)$$

where

$$F_{|i-j|,k}^{\text{anode}} = \frac{\Gamma^2(1/4)}{6\pi^2 \tau_v \sqrt{2k_0}}$$
$$\times \int_0^{\Delta y/2} \left\{ [(x_j - x_0)^2 + (|y_i - y_k| + y')^2]^{-1/4} \right.$$
$$+ [((x_j - x_0)^2 + (|y_i - y_k| - y')^2]^{-1/4}$$
$$- [(x_j - x_0 + \Delta x)^2 + (|y_i - y_k| + y')^2]^{-1/4}$$
$$\left. - [(x_j - x_0 + \Delta x)^2 + (|y_i - y_k| - y')^2]^{-1/4} \right\} dy' \qquad (14)$$

$$F_{|i-j|,k}^{\text{cathode}} = -\frac{\Gamma^2(1/4)}{6\pi^2 \tau_v \sqrt{2k_0}}$$
$$\times \int_0^{\Delta y/2} \left\{ [(x_j - x_{N_x})^2 + (|y_i - y_k| + y')^2]^{-1/4} \right.$$
$$+ [((x_j - x_{N_x})^2 + (|y_i - y_k| - y')^2]^{-1/4}$$
$$- [(x_j - x_{N_x} + \Delta x)^2 + (|y_i - y_k| + y')^2]^{-1/4}$$
$$\left. - [(x_j - x_{N_x} + \Delta x)^2 + (|y_i - y_k| - y')^2]^{-1/4} \right\} dy' \qquad (15)$$

$$F_{|i-j|,k}^{\text{side-walls}} = \frac{\Gamma^2(1/4)}{6\pi^2 \tau_v \sqrt{2k_0}}$$
$$\times \int_0^{\Delta x/2} \left\{ [(|x_i - x_j| + x')^2 + (y_k - y_0)^2]^{-1/4} \right.$$
$$+ [(|x_i - x_j| - x')^2 + (y_k - y_0)^2]^{-1/4}$$
$$- [(|x_i - x_j| + x')^2 + (y_k - y_0 + \Delta y)^2]^{-1/4}$$
$$\left. - [(|x_i - x_j| - x')^2 + (y_k - y_0 + \Delta y)^2]^{-1/4} \right\} dx \qquad (16)$$

Derivation of above relations is presented in "Appendix 2", "Appendix 3" and "Appendix 4" [39].

Photo-degradation of surrounding dielectrics due to UV photons impact

As mentioned above, the excitation coefficient of radiative state for air is assumed to be that representing the second positive system of $N_2(C^3\Pi_u \to B^3\Pi_g)$ [50]. The experimental results reported in literature show that the photon yield from excited electrons of air is between 300 and 406 nm which is equivalent to photon energies between 3.05 and 4.13 eV (UV) [16].

Based on experimental results presented in Fig. 3, around 65.34 % of photons produced due to decay of radiative states of air (nitrogen) have energies more than 3.5 eV [51]. These photons have the ability to break C–C

bonds and thus cause degradation in dielectric. Absorption of radiation is an essential first step to photo-degradation. Strongly absorbed radiation will be attenuated as it passes through the polymer and reaction will be concentrated in the surface layers. The first chemical step in photo-degradation is usually hemolytic bond scission to form free radicals.

Diglycidyl ether of bisphenol-A (DGEBA) is a typical, commercial epoxy resin and is chosen, in this work, as the base material to illustrate the mechanism of damage computation. Figure 4 shows the molecular structure of DGEBA.

Thus, each DGEBA monomer has '14' C–C bonds. The radius of a DGEBA monomer is approximately R (≈ 13.28 Å) [52], and its cross-sectional area is approximately $A_{\text{DGEBA}} = 5.546 \times 10^{-18}$ m^2. The cross-sectional area of the dielectric anode is $A_{\text{anode}} = A_{\text{cathode}} = L_y \times L_z$ and the area of each side-wall is $A_{\text{side-walls}} = L_x \times L_z$. The number of DGEBA monomers on the surface of the dielectric anode and cathode is thus approximately $(N_{\text{DGEBA}})_{\text{anode}} = (N_{\text{DGEBA}})_{\text{cathode}} = A_{\text{anode}}/A_{\text{DGEBA}}$, and that on the surface of side-wall is $(N_{\text{DGEBA}})_{\text{side-walls}} = A_{\text{side-walls}}/A_{\text{DGEBA}}$. If N_{CC} is number of C–C bonds which can be broken during one PD pulse, then the total pulses required to break all C–C bonds existing on the dielectric anode, cathode and side-walls (N_{pc}) are as follows:
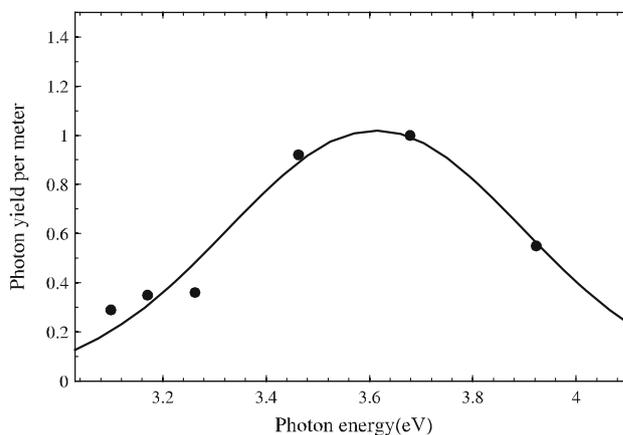
Fig. 3 Schematic representation of photon yield per unit length per electron [16]
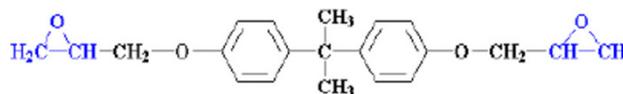
Fig. 4 Molecular formulae of DGEBA monomer

Table 1 Simulation data

Property	Symbol	Value
Narrow channel length	L_x	20 μm
Narrow channel width	L_y	1 μm
Narrow channel depth	L_z	1 μm
Dielectric thickness	L_d	20 μm
Background gas pressure	P_g	101,325 Pa
Background gas temperature	T_g	0.026 eV
External capacitor	C	40 pF
Initial number of charged particles	n_f	10
Photo-emission coefficient	λ_{ph}	5×10^{-5} [58]
Ion-induced emission coefficient	λ_i	1.5×10^{-3} [58]
Dielectric constant of air	ε_0	8.85×10^{-12} F/m
Linewidth (FWHM of the line shape)	$\Delta \upsilon^L$	2.9435 GHz
Wavelength at the line center	λ_0	5 nm
Vacuum radiative decay time	τ_υ	40 ns
Degeneracy of lower state	g_1	1
Degeneracy of lower state	g_2	3

$$(N_{pc})_{anode} = 14 \times (N_{DGEBA})_{anode} / (N_{CC})_{anode}$$
$$(N_{pc})_{cathode} = 14 \times (N_{DGEBA})_{cathode} / (N_{CC})_{cathode}$$
$$(N_{pc})_{side-walls} = 14 \times (N_{DGEBA})_{side-walls} / (N_{CC})_{side-walls}$$
$$(17)$$

Here $(N_{pc})_{anode}$, $(N_{pc})_{cathode}$ and $(N_{pc})_{side-walls}$ are the total pulses required to break all C–C bonds existing on the surface of dielectric anode, cathode and side-walls.

The total number of cycles required to break all C–C bonds on surrounding dielectrics of narrow channel may be obtained as follows:

$$(N_{cycle})_{anode} = (N_{pc})_{anode} / N_{PDC}$$
$$(N_{cycle})_{cathode} = (N_{pc})_{cathode} / N_{PDC}$$
$$(N_{cycle})_{side-walls} = (N_{pc})_{side-walls} / N_{PDC}$$
$$(18)$$

Here $(N_{cycle})_{anode}$, $(N_{cycle})_{cathode}$ and $(N_{cycle})_{side-walls}$ are the total number of required cycles to break all C–C bonds on the surface of dielectric anode, cathode and side-walls, where N_{PDC} indicates the number of PD pulses per cycle [53–57].

So, the time required to break all C–C bonds on the surface of surrounding dielectrics of narrow channel (t_{cc}) at a supply frequency of 50 Hz ($T = 20$ ms) can be calculated as follows:

$$(t_{cc})_{anode} = T \times (N_{cycle})_{anode}$$
$$(t_{cc})_{cathode} = T \times (N_{cycle})_{cathode}$$
$$(t_{cc})_{side-walls} = T \times (N_{cycle})_{side-walls}$$
$$(19)$$

Here $(t_{cc})_{anode}$, $(t_{cc})_{cathode}$ and $(t_{cc})_{side-walls}$ are the times required to break all C–C bonds on surface of dielectric anode, cathode and side-walls.

Simulation results

The simulation results of the two-dimensional RT-PIC model are presented here. The results of the effect of several factors like the applied electric field, channel dimensions and gas pressure on the extent of degradation of dielectric anode, cathode and side-walls, due to C–C bond break by UV photon impact, are presented in the following sections. Results are presented here with simulation parameters presented in Table 1. It may be noted that a channel with a significantly large length/width ratio is chosen.

The scatter plots in phase space for velocities in x-direction i.e. (V_x, x, y) for electrons, and positive ions inside the micro-channel are shown in Figs. 5 and 6 at particular instants of time. As shown here, drift velocity of electrons is much greater than that of ions (3 orders of magnitude higher) and quickly traverse the micro-channel length. All charged particles are distributed about the center-line $y = 50$ μm. Most of charged particles are created very close to the anode. The number of ions near the anode increases through ionization with passage of time. The positive ions slowly drift towards the cathode, till at about 600 ps the entire gap distance is almost evenly populated. From this time onwards, ions gradually leave the channel, thus depleting the ion density in the gap. This is similar to the evolution of the electrons within the gap, as seen in Fig. 5, except that electrons move faster and need travel only a small distance between the ionization region and the anode. As is clear from Fig. 6, ion velocities increase as they reach near the cathode, accelerated by the electric field. Generally, owing to high electric field strength along micro-channels, attachment process is weak and the production of negative ions is low.

The spatial variation of the x-component of electric field ($E_x(x,y)$) is depicted in Fig. 7. The distribution of field within the narrow channel is originally uniform. The distribution of charged particles inside the narrow channel (in Figs. 5, 6) shows that the effect of space charge on applied field is mostly due to positive ions. A positive space charge region forms ahead of the anode where they accumulate. This results in a reduced field close to the anode. Simultaneously the field near the cathode is enhanced in the direction of the applied field, due to the positive charge cloud now nearing the negatively charged cathode. Owing to the accumulation of negatively charged particles at the anode which causes the anode potential to reduce, the field at the anode never recovers original values. Finally, the field within the channel becomes uniform as the charge dissipates.

Applied electric field

In this subsection, the effect of applied electric field on the extent of degradation of dielectrics surrounding the narrow

Fig. 5 Scatter plot of electrons in the phase-space (V_x, x, y) inside the micro-channel at particular instants of time
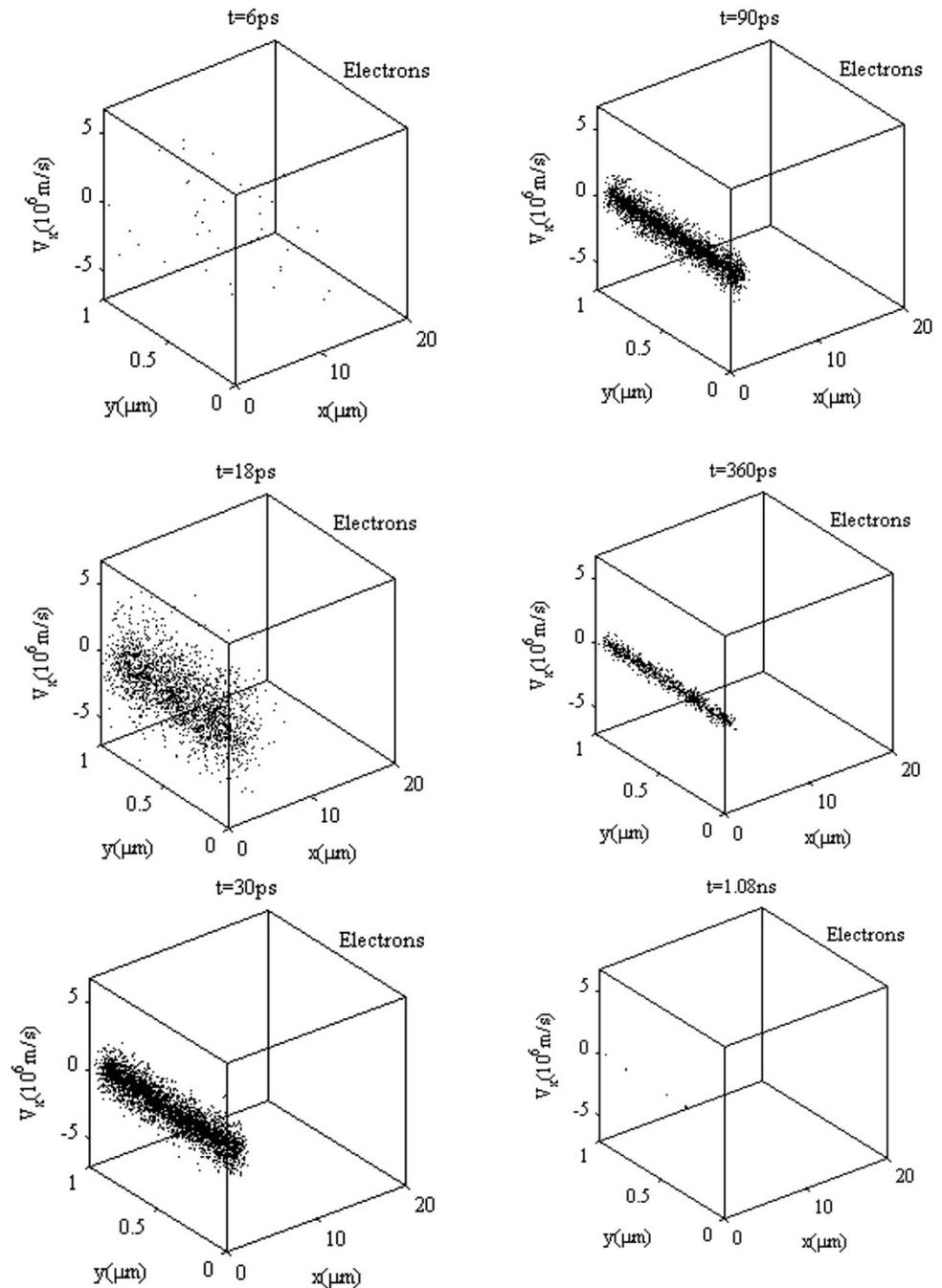
channel based on C–C bonds broken by PD pulses inside the narrow channel is studied.

As electric field across narrow channel increases, ionization increases and consequently there is an increase in the number of excited states (radiative states) inside the narrow channel. Thus not only the total number of electrons, but additionally the number of UV photons reaching the surrounding dielectrics increases. As described before, every DGEBA monomer has '14' C–C bonds; photons and electrons with energies higher than 3.5 eV are capable of

breaking these molecular bonds. The number of broken C–C bonds during a single PD pulse (N_{CC}) by electrons and photons are depicted in Fig. 8. Figure 8a shows the impact of electrons is higher on the dielectric anode than on the side-walls, while photons have a greater effect on side-walls than on anode, as seen in Fig. 8b. This is because in the current simulation, the ratio of length to width (20) is high and this causes a larger number of photons to reach the dielectric side-walls rather than the anode or cathode. Generally, propagation of photons inside the micro-channel

Fig. 6 Scatter plot of positive ions in the phase-space (V_x, x, y) inside the micro-channel at particular instants of time
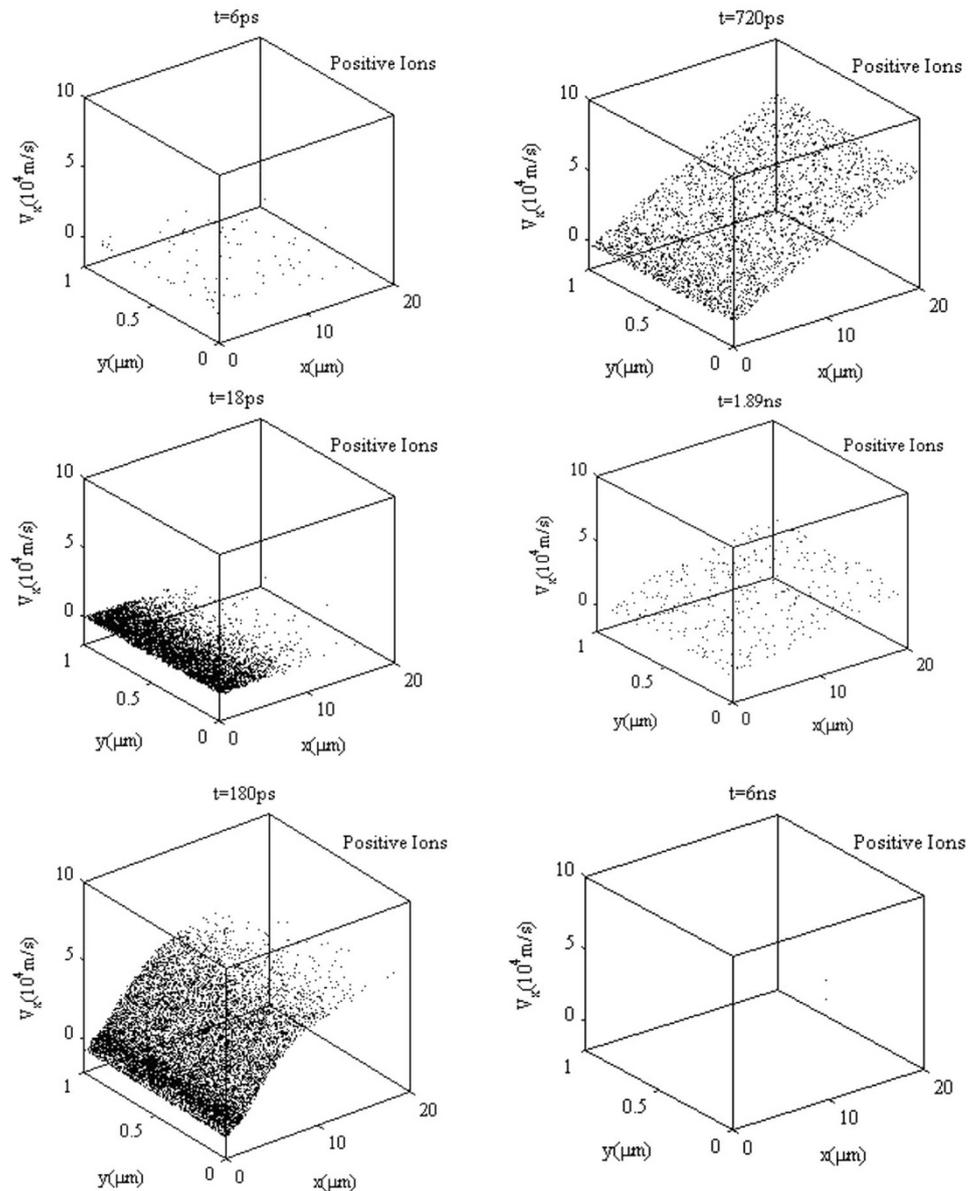
is not determined by the applied electrostatic field due to their mass-less and charge-less nature, while charged particle movement is governed by fields. Thus photons are likelier to reach the side-walls rather than the ends of the narrow channel, as that entails lesser distance of travel. Therefore, the side-walls are overwhelmingly likely to undergo photo-degradation. Interestingly, as shown in Fig. 8, the value of N_{CC} due to UV photons is almost 1,000 higher than due to electrons. Hence, the resultant degradation based on C–C bond-break due to the effect of electrons is negligible.

As seen in Fig. 9a, the time required to break all the existing C–C bonds (t_{cc}) on the surface of dielectrics surrounding the narrow channel varies considerably with

electric field. An increase of electric field from 8 to 50 kV/mm causes t_{cc} to vary from 347 to 0.2121 ms for the dielectric anode, 248 to 0.1102 ms for the dielectric side-walls and 618 to 0.4537 ms for dielectric cathode. Figure 9b through d show the temporal variation in the number of UV photons reaching the dielectric anode, cathode and side-walls for different values of applied electric field. We see a higher number of UV photons at higher fields. Tanaka et al. [59] have shown that for a cavity with a diameter of 5 mm, the intensity of light emitted from a discharge within the cavity decreases with decrease in applied voltage.

It may be noted that the light emission from PD activity gives us information about spatial distribution of PD in

Fig. 7 Spatial variations of
x-component of electric field
($E_x(x,y)$) inside the narrow
channel at different time
moments
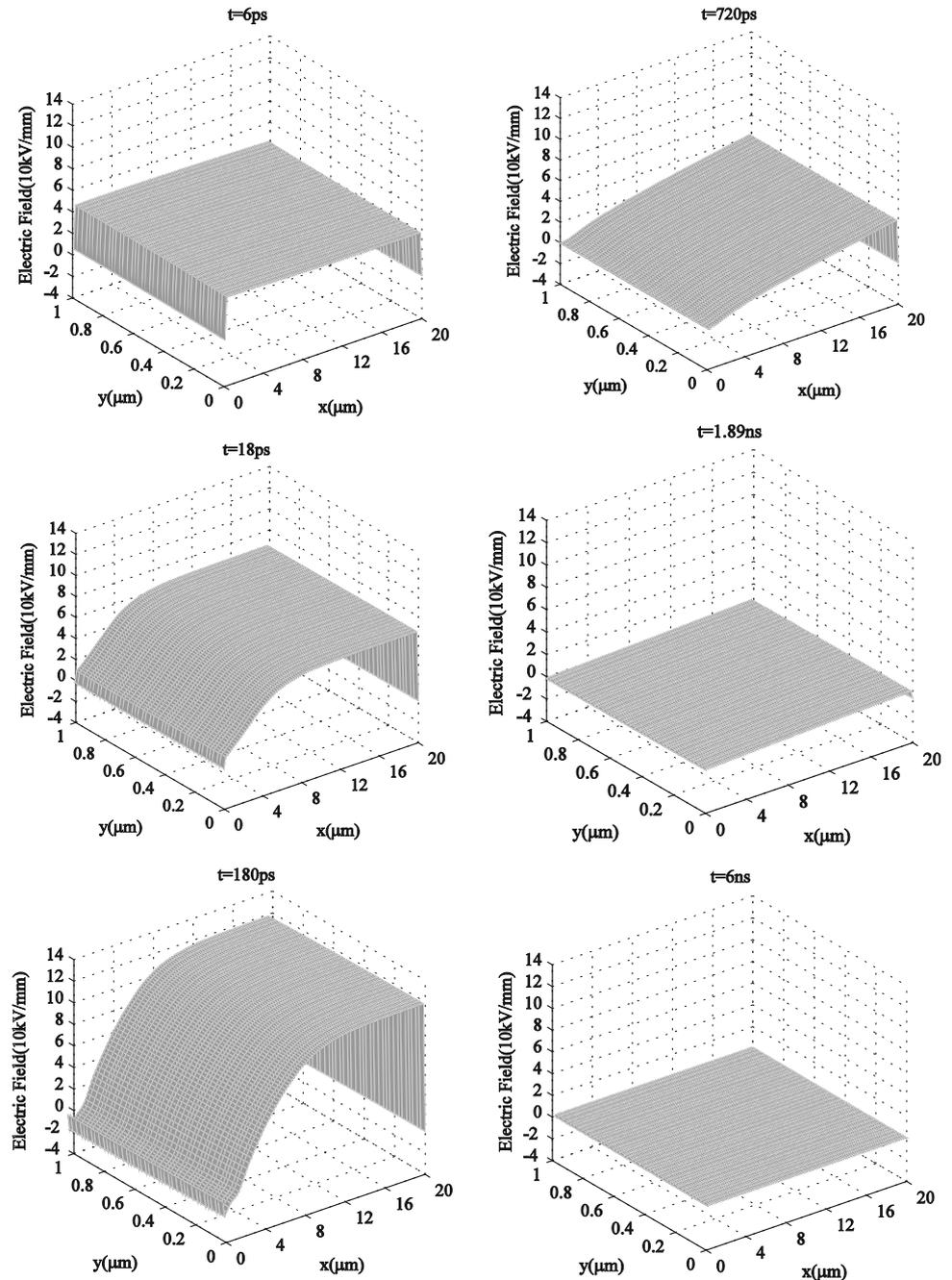
narrow channels. Figures 10, 11, 12 and 13 show that the radiative states (or photons) inside the narrow channel are mostly concentrated near the anode (ionization region). We see that with increase in electric field, the region of production and concentration of photons moves further towards the dielectric anode.

Laurent et al. [5] stated that because of the very small sizes of narrow channels, the results of the discharge physics for plane, parallel, metallic electrodes may not be easy to predict. It might not be possible to know definitely whether discharges would develop between or along the walls of the channel [60].

Our results corroborate the observations of Kaneiwa et al. [10]. They noted that light emission occurred due to PD in an artificial channel before a new narrow channel propagated. At lower applied voltage of 3 kV, light emission mainly occurs near the needle tip. At higher applied voltage of 6 kV, the light emission extended to the vicinity of channel tip.

Champion et al. [61] developed a partial discharge model (a pin-plane electrode arrangement) to simulate

(a)

(b)
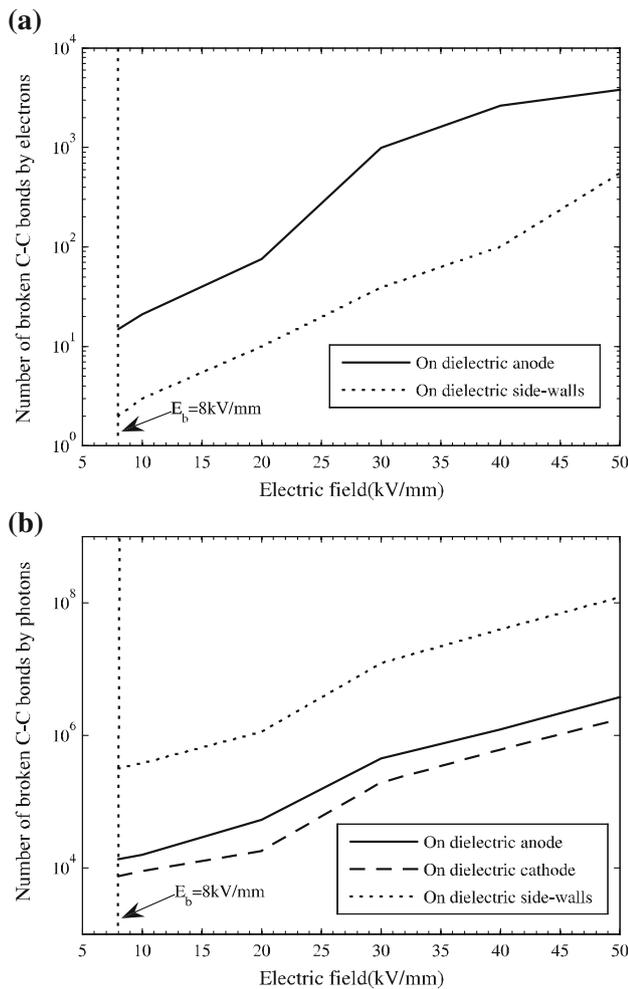
Fig. 8 Total number of broken C–C bonds during one PD pulse (N_{CC}) by **a** electrons, **b** photons

experimental partial discharge activity within electrical tree (narrow channel) structures grown in polymer based insulation. They also simulated partial discharges within an arbitrarily defined non-conducting electrical tree structure [62]. They report that the light emitted from partial discharge activity was initially observed from the whole tree structure. The photographs of light emission due to a PD pulse in an artificial tree channel of 5 mm length reported by Wu et al. [12] show that the region of light emission becomes larger at higher voltages. They report that the light is brighter near the needle tip and the region of light emission is much shorter than the channel length, i.e. light emission takes place only in a part of the channel closer to the needle electrode.

Micro-channel length

In this section, the effect of narrow channel length on the degradation of surrounding dielectrics due to PD pulse

inside the narrow channel based on the C–C bond break is considered. Simulations are performed for the operating parameters presented in Table 1.

As a single electron traverses larger distances between the dielectric electrodes in larger narrow channels, with increase in narrow channel length (applied electric field remaining the same), greater amounts of excitation, ionization and attachment occur due to larger number of collisions per electron. Increase in number of excitation collisions leads to increase in the total number of radiative states and consequently the number of UV photons reaching the dielectrics surrounding the narrow channel. Thus, as seen in Fig. 14a, with increase in length the time required to break all existing C–C bonds (t_{cc}) reduces. Noskov et al. [63] developed a self-consistent model for electrical tree propagation and PD activity within narrow tree channels and showed that the magnitude of individual PD event increases with the narrow channel length.

Temporal variations in the total number of UV photons reaching the dielectric anode, cathode and side-walls for specific narrow channel lengths are presented in Fig. 14b through d. As seen in these figures, the number of UV photons reaching the surrounding dielectrics is higher at greater channel lengths. The total number of UV photons arriving at the surface of dielectric side-walls is an order of magnitude higher than at the dielectric anode and two orders of magnitude greater than at dielectric cathode.

As seen in Figs. 15, 16 and 17, as the narrow channel length increases, the region where the UV photons are mostly produced moves towards the dielectric anode. Also the size of this region increases with channel length, and the photons are distributed over a wider area within the narrow channel. As may be seen, for the channel length of $L_x = 10$ μm, the order of radiative states (photons) is 10^{-18} m^{-3} and is mostly concentrated around $x/L_x = 0.3$, while for greater narrow channel lengths, i.e. $L_x = 25$ μm, the order of radiative states is 10^{-20} m^{-3} and with a wider distribution which is concentrated around $x/L_x = 0.04$.

Width

The effect of width is studied in this subsection. The simulation is performed for the operating parameters in Table 1.

With increase in width of narrow channel, the likelihood of random movement of charge carriers in a direction perpendicular to the applied electric field (y-direction) increases [64]. Hence, the rate of ionization, as the charges move under the influence of the electric field, is lower [20]. The likelihood of excitation reduces. Due to decrease in the number of exciting collisions, the density of radiative states and consequently the number of UV photons reaching the surrounding dielectrics decreases. Thus, as is depicted in
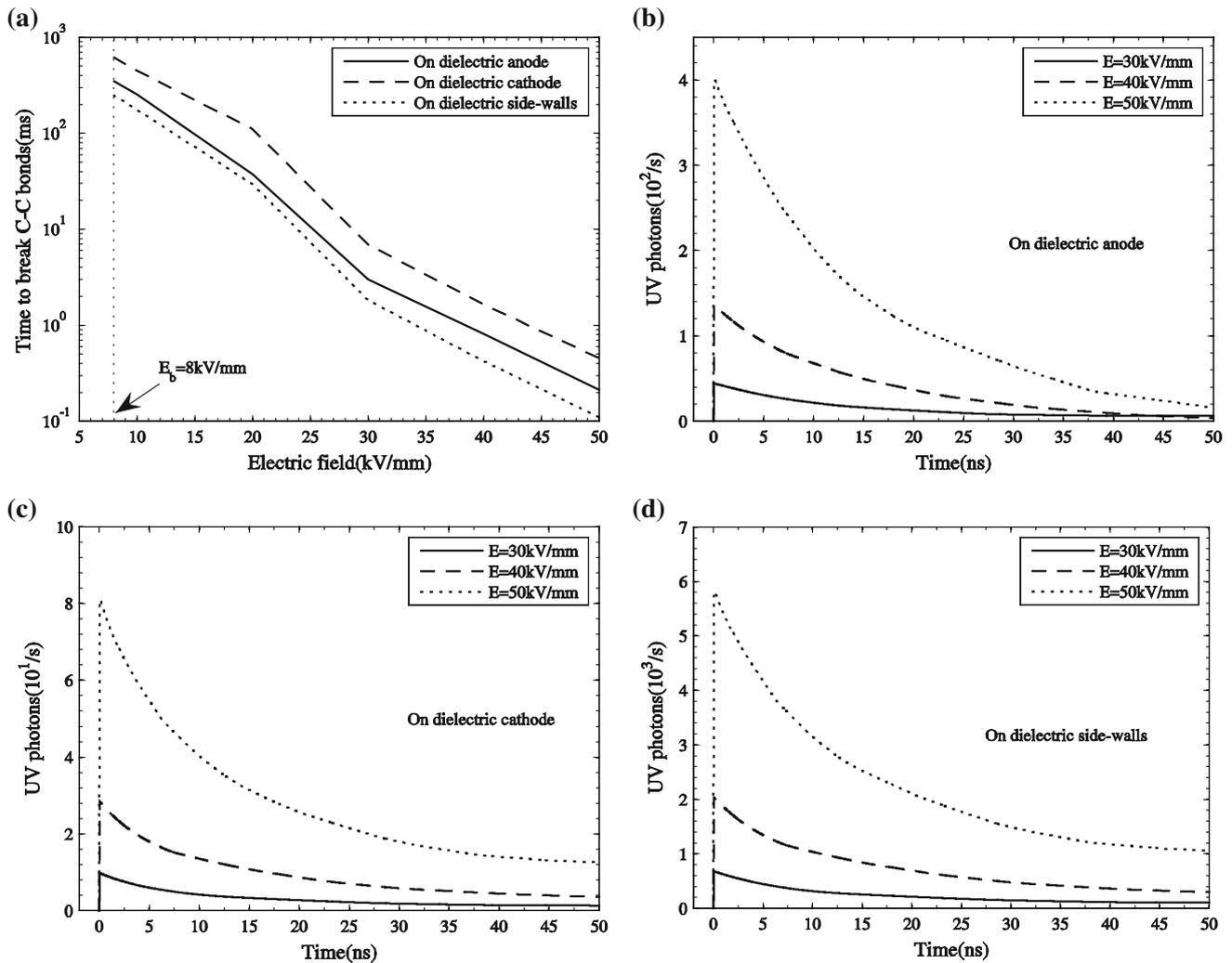
Fig. 9 **a** Time required to break all C–C bonds (t_{cc}) on surrounding dielectrics as a function of applied electric field across the narrow channel, and the time history of total amount of UV photons arriving dielectric, **b** anode, **c** cathode, **d** side-walls for three different values of applied electric field

Fig. 18a, the time required to break all the existing C–C bonds (t_{cc}) increases as width of narrow channel increases. Figure 18a shows that for channel widths below 2 μm, the value of t_{cc} for dielectric side-walls is lower than for dielectric cathode. Thus, the effect of width appears to be similar to the effect of electric field, as seen before. But above 2 μm, the value of t_{cc} for dielectric side-walls is higher. As mentioned earlier, the movement of photons is not affected by applied electrostatic field, and they are likely to travel radially outwards from the site of production. In doing so, at greater narrow channel widths, the probability of such photons reaching the side-walls rather than the anode or even the cathode is lower. This would explain the above observation.

The effect of reduced excitation is lower production in radiative states (UV photons) in the narrow channel for wider narrow channels, from 10^{-19} m^{-3} for $L_y = 2$ μm to 10^{-15} m^{-3} for $L_y = 80$ μm, as seen in Figs. 19, 20 and 21. A comparison of Figs. 19 and 20 shows that photons are concentrated mostly around $x/L_x = 0.2$ for $L_y = 2$ μm and $x/L_x = 0.6$ for $L_y = 80$ μm inside the narrow channel. It may be concluded that the region of concentration of UV photons is seen to be located far away from the anode at greater narrow channel widths.

Pressure

Generally, gas pressure inside the narrow channel has considerable effect on the light emitted from gaseous discharges. In this subsection we investigate the effect of gas pressure inside the narrow channel. The simulation is

(a)

(b)
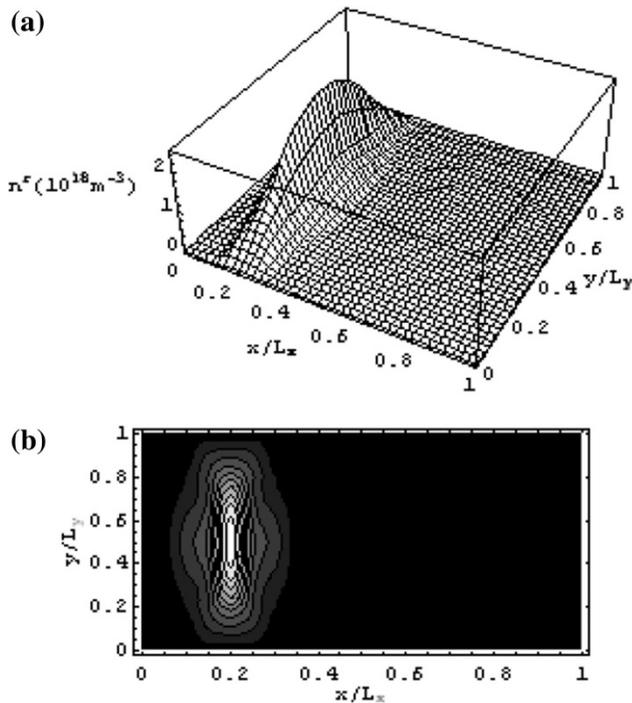
Fig. 10 **a** Surface plot and **b** contour map of radiative states (average respect to time) inside narrow channel; applied field across narrow channel $E = 20$ kV/mm, narrow channel length $L_x = 20$ μm, narrow channel width $L_y = 1$ μm, gas pressure inside narrow channel $P_g = 760$ Torr

(a)

(b)
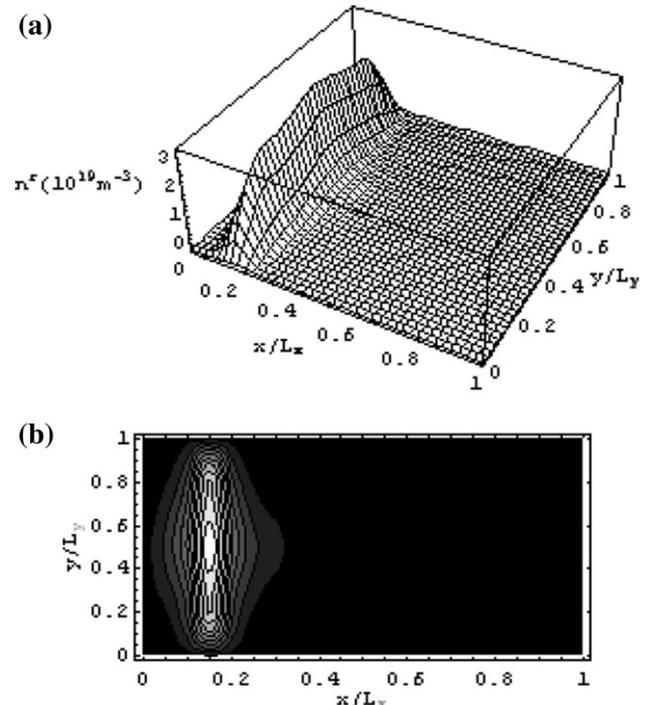
Fig. 11 **a** Surface plot and **b** contour map of radiative states (average respect to time) inside narrow channel; applied field across narrow channel $E = 30$ kV/mm, narrow channel length $L_x = 20$ μm, narrow channel width $L_y = 1$ μm, gas pressure inside narrow channel $P_g = 760$ Torr

performed for the operating parameters presented in Table 1.

The ionization process and consequent production of new electrons in partial discharges is affected by change in pressure of gas due to its direct effect on the probability of collision of charged particles with neutrals. Just as an increase in gas pressure causes greater ionization of neutrals, so does it cause a number of excited (radiative) states or UV photons to be produced inside the narrow channel and thus a larger number reaches the surrounding dielectrics. As a result, as shown in Fig. 22a, with increase in gas pressure inside the narrow channel, the time required to break all the existing C–C bonds (t_{cc}) by photon impact reduces.

Figure 22b through d show the temporal variations of the total number of the UV photons reaching the dielectric anode, cathode and side-wall surfaces for three different values of gas pressure inside narrow channel. The total number of UV photons reaching the dielectrics surrounding the narrow channel is higher at higher pressures.

As seen in Figs. 23, 24 and 25, region of concentration of radiative states or UV photons inside the narrow channel occurs nearer the anode at higher pressures. Also, the UV photons inside the narrow channel are distributed over a more extensive region at higher pressures.

Discussion

From the results presented in this paper, we see that the impact of electrons on dielectric anode is significantly more than on side-walls. In contrast, the UV photons impact predominantly on the dielectric side-walls.

We have shown that the UV photons are mainly produced in ionization region and around $y = 0.5$ μm and production decreases nearer the dielectric side-walls as well as dielectric anode and cathode.

Increase in applied electric field, micro-channel length and gas pressure, and decrease in channel width cause an increase in the total number of UV photons reaching the dielectric anode. This is due to increased amount of excitation of neutrals inside the narrow channel. This leads to greater cumulative degradation of surrounding dielectrics over time.

Dissociation of C–C bonds can reduce progressively the mass of the fragments of epoxy that eventually may deteriorate the insulation. Moreover, cross-linking between different chains holding free radicals can occur, along with oxidation and graphitization or other chemical reactions. These processes are triggered by a production of such radicals and double bonds on the surrounding dielectrics of narrow tree channel under the action of energetic charged

(a)

(b)
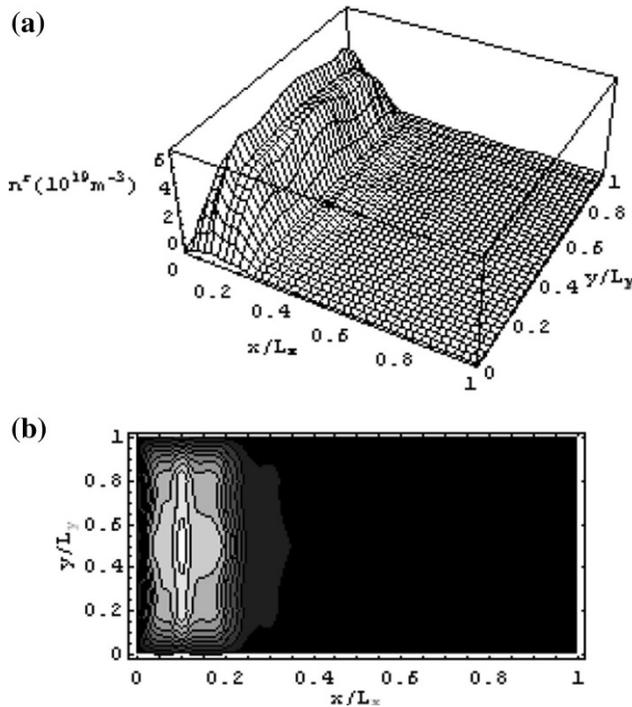
Fig. 12 **a** Surface plot and **b** contour map of radiative states (average respect to time) inside narrow channel; applied field across narrow channel $E = 40$ kV/mm, narrow channel length $L_x = 20$ μm, narrow channel width $L_y = 1$ μm, gas pressure inside narrow channel $P_g = 760$ Torr

(a)

(b)
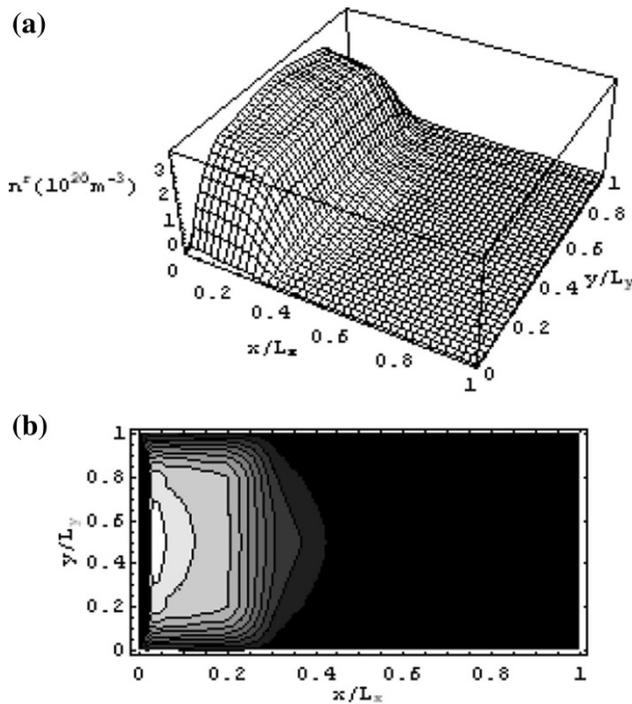
Fig. 13 **a** Surface plot and **b** contour map of radiative states (average respect to time) inside narrow channel; applied field across channel $E = 50$ kV/mm, channel length $L_x = 20$ μm, channel width $L_y = 1$ μm, gas pressure inside channel $P_g = 760$ Torr

particles and UV photons produced during PD process. Unfortunately, experimental data for C–C dissociation cross-sections and the other possible chemical reactions are not readily available in literature. Thus, the studies undertaken in this work provide a comparative analysis of the general manner in which various parameters affect degradation due to photon impact, rather than an exact quantitative analysis.

Conclusion

The RT-PIC model presented in this paper successfully reproduces the salient features of light emission during PD pulse within a narrow channel, and yields detailed information about the extent of C–C bond breakage. This gives us information about the extent of degradation of the surrounding dielectrics due to UV photon impacts produced by PD pulses. C–C bond breaks due to impact of electrons is negligible and is mainly related to photo-degradation.

Appendix 1: Electrostatic equations for dielectric narrow channel

The total charge density σ_T on the anode metallic electrode may be expressed by [21]:

$$\sigma_T^t = \sum_{j=0}^{N-1} \sigma_{0j}^t \qquad (20)$$

where σ_{0j}^t is the surface charge density on anode electrode at time 't'. The simplified form of equation (26) of [21] for a 'simple metallic-metallic' configuration (ref. [20]) is:

$$\sigma_T^t = \frac{\varepsilon_0}{\Delta x} N \varphi_0^t - \frac{\varepsilon_0}{\Delta x} \sum_{j=0}^{N-1} \varphi_{1j}^t - \frac{\Delta x}{2} \sum_{j=0}^{N-1} \rho_{0j} \qquad (21)$$

where, $\varphi_0^t, \varphi_{1j}^t$, N are the potential on the anode at 't', potential at $x_1 (=1 \times \Delta x)$ and number of divisions along y-axis. Particle 'p' contributes to Q_{ij} through the space charge density ρ_{ij} (bilinear weighting: [21]).

The equivalent circuit for the narrow channel bounded by dielectrics is shown in Fig. 2b. C_g, C_d and C_r represent the equivalent capacitances of the gap, the dielectric layers and dielectric material parallel to the micro-channel respectively, and J_{conv} is the discharge current density. The time variation of σ_T, the total charge density on the driven
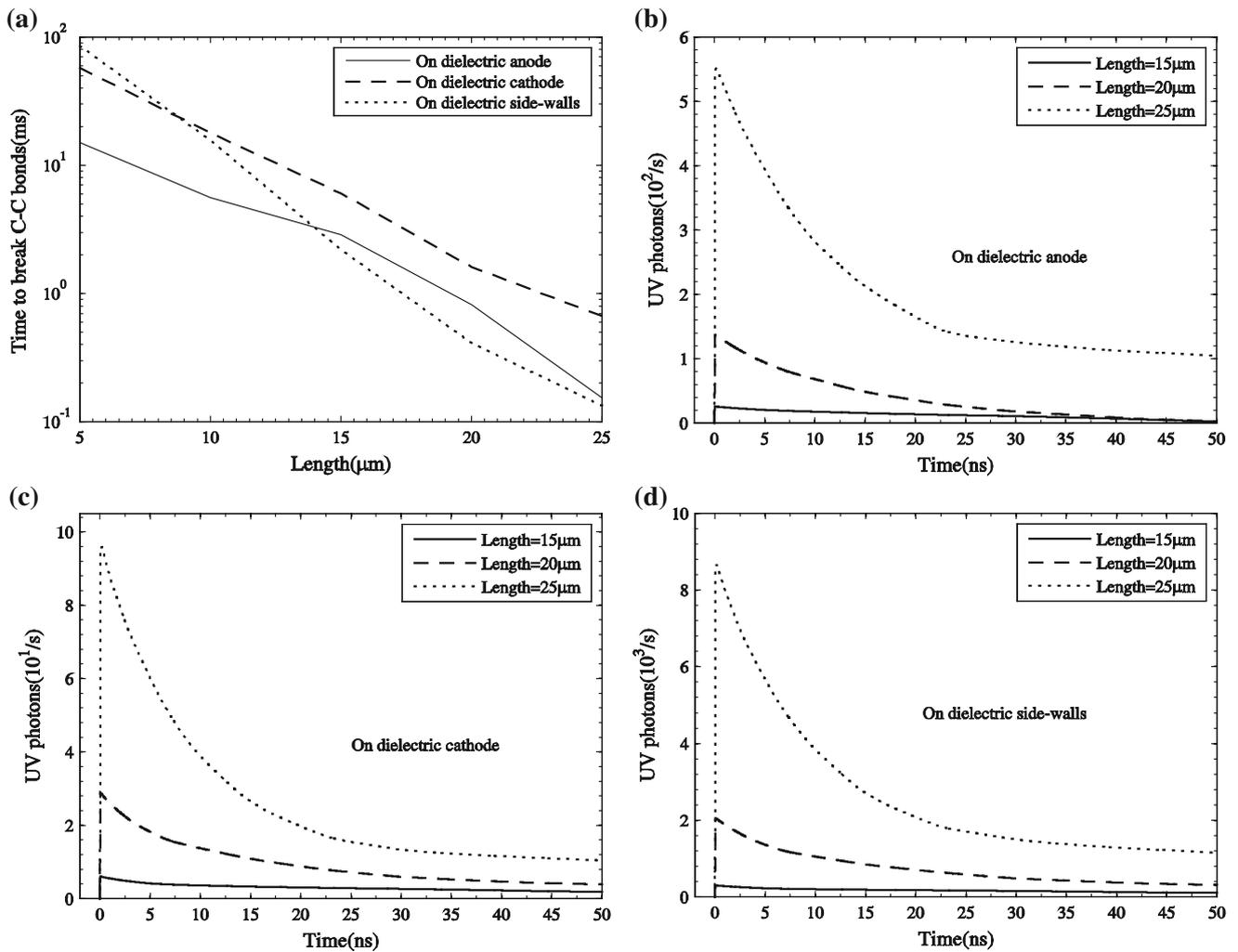
Fig. 14 **a** Time required to break all C–C bonds (t_{cc}) on surrounding dielectrics versus length of narrow channel, and the time history of total amount of UV photons arriving dielectric, **b** anode, **c** cathode, **d** side-walls for three different values of narrow channel length

dielectric electrode, may be obtained from the Kirchhoff's Current Law:

$$A\frac{d\sigma_s}{dt} = I_{ext} - I_r + AJ_{conv}, \tag{22}$$

where I_{ext}, σ_T and I_r the total external current, charge on the dielectric surfaces and current in the dielectric material parallel to the narrow channel.

The time variation of voltage drop (U_d) across the dielectric slab is obtained as:

$$C_d\frac{dU_d}{dt} = I_{ext} - I_r. \tag{23}$$

Figure 2b shows a simple external circuit consisting of a voltage source in series with a capacitor coupled to the left electrode. The voltage drop V_c across the capacitor in the external circuit is obtained from voltage balance as,

$$V_c = V(t) - 2U_d - \varphi_0 \tag{24}$$

$V(t)$ is the applied voltage source. The discrete finite differenced form of (23) can be expressed as:

$$A(\sigma_T^t - \sigma_T^{t-1}) = Q_c^t - Q_c^{t-1} - Q_r^t + Q_r^{t-1} + Q_{conv}^t \tag{25}$$

where $\int I dt = Q_c = CV_c$ and $\int I_r dt = Q_r = CU_r$ and are the charge on the external capacitor and bulk of dielectric material parallel to the narrow channel, and Q_{conv}^t is the charge deposited on the electrode from the discharge in the cavity during the time interval $(t - 1, t)$. Combining Eqs. (24) and (25), the following relation can be obtained:

$$\sigma_T^t = \sigma_T^{t-1} + \frac{1}{A}(CV(t) - (C + C_r)\varphi_0^t$$
$$- 2(C + C_r)U_d^t + Q_r^{t-1} - Q_c^{t-1} + Q_{conv}^t) \tag{26}$$

Similarly, the discrete finite differenced form of (23) can be expressed as:

(a)

(b)
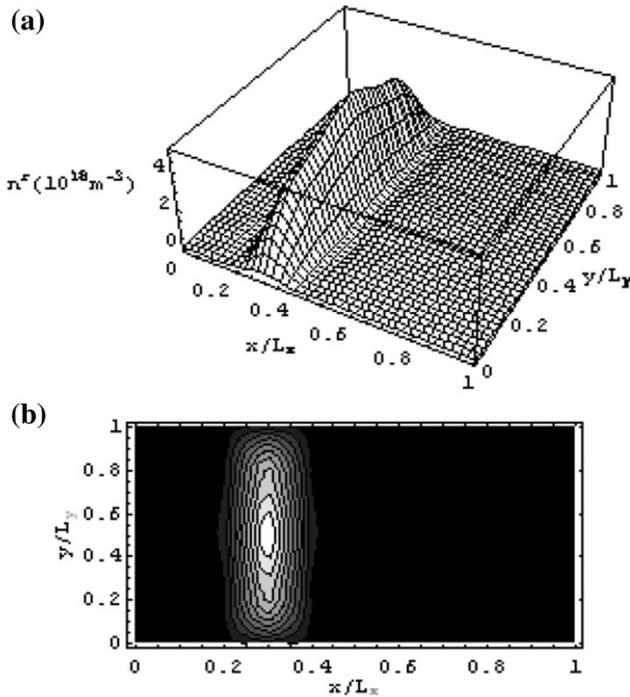
Fig. 15 **a** Surface plot and **b** contour map of radiative states (average respect to time) inside the narrow channel; applied field across narrow channel $E = 40$ kV/mm, narrow channel length $L_x = 10$ μm, narrow channel width $L_y = 1$ μm, gas pressure inside narrow channel $P_g = 760$ Torr

$$U_d^t - U_d^{t-1} = \frac{1}{C_d} \int (I_{ext} - I_r)dt = \frac{Q_c^t - Q_c^{t-1} - Q_r^t + Q_r^{t-1}}{C_d}$$

(27)

If Eqs. (24) and (27) are combined, then we have:

$$U_d^t = \frac{U_d^{t-1} + \frac{1}{C_d}(CV(t) - (C + C_r)\varphi_0^t - Q_c^{t-1} + Q_r^{t-1})}{1 + (C + C_r)/C_d}$$

(28)

By inserting the value of U_d^t to the Eq. (26) and taking $\alpha = (1 + 2(C + C_r)/C_d)^{-1}$, the value of σ_T^t can be written as follow:

$$\sigma_T^t = \sigma_T^{t-1} + \frac{1}{A}(\alpha CV(t) - \alpha(C + C_r)\varphi_0^t -$$
$$2\alpha(C + C_r)U_d^{t-1} - \alpha Q_c^{t-1} + \alpha Q_r^{t-1} + Q_{conv}^t)$$

(29)

Equations (20), (21) for σ_T^t and (29) can be combined and solved for φ_0^t on dielectric anode to produce:

$$\varphi_0^t = \left(\sigma_{s_T}^{t-1} + \frac{1}{A}(\alpha CV(t) - \alpha Q_c^{t-1} + \alpha Q_r^{t-1} \right.$$
$$\left. - 2\alpha(C + C_r)U_d^{t-1} + Q_{Conv}^t) + \frac{\Delta x}{2}\sum_{j=0}^{j=N}\rho_{0j} + \frac{\varepsilon}{\Delta x}\sum_{j=0}^{j=N}\varphi_{1j}^t \right)$$
$$\left(\frac{\varepsilon}{\Delta x}N + \alpha(C + C_r)/A \right)^{-1}$$

(30)

(a)

(b)

Fig. 16 **a** Surface plot and **b** contour map of radiative states (average respect to time) inside narrow channel; applied field across narrow channel $E = 40$ kV/mm, narrow channel length $L_x = 15$ μm, narrow channel width $L_y = 1$ μm, gas pressure inside narrow channel $P_g = 760$ Torr

Appendix 2: Derivation of radiation transport matrix

The probability of a photon emitted at $\acute{r}$ within the (j,k)th cell to be reabsorbed at the center of the (j,k)th cell, r_{jk}, is defined as

$$A_{jk;lm} = \int_{lm} G(r_{jk}, r')dr'$$

(31)

where $\int_{lm} dr'$ is a volume integral over the (l,m)th cell, and the kernel function $G(r,\acute{r})$ is calculated from the transmission factor as

$$G(r,r') = -\frac{R}{4\pi R^3} \cdot \nabla_r T(r,r')$$
$$= -\nabla_r \cdot \left[\frac{R}{4\pi R^3} T(r,r') \right] + \delta^3(r,r')$$

(32)

With uniform ground-state density profile, the line shape, $g(v, r)$, and the absorption coefficient, $k(v, r)$, depend only on frequency of the photons, v, and thus the transmission factor is

$$T(R) = \int_0^\infty g(v)e^{-k(v)R}dv$$

(33)

(a)

(b)
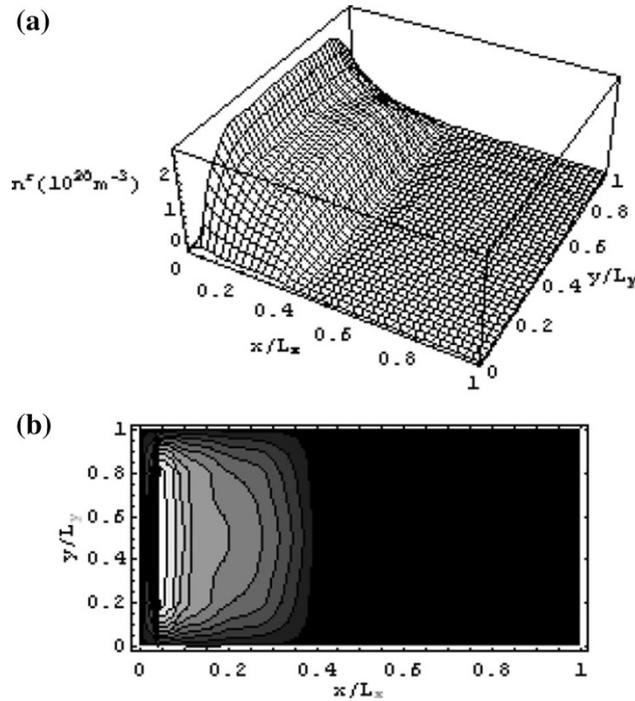
Fig. 17 **a** Surface plot and **b** contour map of radiative states (average respect to time) inside narrow channel; applied field across narrow channel $E = 40$ kV/mm, narrow channel length $L_x = 25$ μm, narrow channel width $L_y = 1$ μm, gas pressure inside narrow channel $P_g = 760$ Torr

where $R = |r - \acute{r}|$. Pressure broadening which has the Lorentz line shape is the dominant broadening mechanism in a PDP cell, and for this case, Eq. (33) becomes [34]:

$$T(R) = \frac{\Delta v}{2\pi} \int_0^\infty dv \frac{1}{(v - v_0)^2 + (\Delta v/2)^2}$$
$$\times \exp\left(-\frac{k_0 R}{4(v - v_0)^2 / \Delta v^2 + 1}\right) \quad (34)$$
$$= \exp\left(-\frac{k_0 R}{2}\right) I_0\left(\frac{k_0 R}{2}\right)$$

where $I_0(x)$ is the zeroth-order modified Bessel function. The equation can be approximated at high opacity ($k_0 R \gg 1$) as

$$T(R) \cong \frac{1}{\sqrt{\pi k_0 R}} \quad (35)$$

From Eq. (32) with divergence theorem

$$A_{jk;lm} = \delta_{jl}\delta_{km} + \int_{lm} \frac{T(r_{jk}, r')}{4\pi R^3} R \cdot \hat{n} dS \quad (36)$$

The surface integral in Eq. (36) has four segments in Cartesian coordinates as shown in Fig. 26, and each of them is defined as $A_{jk;lm}^{(a)}$, $A_{jk;lm}^{(b)}$, $A_{jk;lm}^{(c)}$ and $A_{jk;lm}^{(d)}$.

With the property of shift invariance and isotropy, it has been verified that $A_{jk;lm}$ is only a function of the distance

between the positions of photon emission and re-absorption, and thus $A_{jk;lm} = A_{|j-l|,|k-m|}$. For the top boundary in Fig. 26:

$$A_{jk;lm}^{(a)} = \left(y_k - y_m - \frac{\Delta y}{2}\right) \int_{x_l - \Delta x/2}^{x_l + \Delta x/2} dx' \int_{-\infty}^{\infty} \frac{T(R)}{4\pi R^3} dz'$$
$$= -\frac{\Delta y}{2\pi}\left(|k - m| + \frac{1}{2}\right) \int_{x_l - \Delta x/2}^{x_l + \Delta x/2} dx'$$
$$\times \int_0^{\pi/2} \cos\theta \, d\theta \frac{T(R_\perp \sec\theta)}{R_\perp^2} \quad (37)$$

where $R_\perp = R\cos\theta = [(x_j - x')^2 + (y_k - y_m - \Delta y/2)^2]^{1/2}$ and $z = R_\perp \tan\theta$. With the high opacity approximation, Eq. (35)

$$A_{|j-l|,|k-m|}^{(a)} = -\frac{\Delta y}{2\pi}(|k - m| + 1/2)\frac{1}{\sqrt{\pi k_0}}$$
$$\times \int_{x_l - \Delta x/2}^{x_l + \Delta x/2} \frac{1}{R_\perp^{5/2}} dx' \int_0^{\pi/2} \cos^{3/2}\theta \, d\theta$$
$$= -\frac{\Delta y(|k - m| + 1/2)}{12\pi^2\sqrt{2k_0}}\Gamma^2(1/4)$$
$$\times \int_{(|j-l|-1/2)\Delta x}^{(|j-l|+1/2)\Delta x}\left[x^2 + \Delta y^2(|k - m| + 1/2)^2\right]^{-5/4} dx \quad (38)$$

which is a single integral over position x. Here, $\Gamma(1/4) = 3.6256$ is a specific value of the gamma function and comes from the relation

$$\int_0^{\pi/2} \cos^{3/2}\theta \, d\theta = \frac{1}{6\sqrt{2\pi}}\Gamma^2(1/4) \quad (39)$$

For the bottom boundary

$$A_{|j-l|,|k-m|}^{(c)} = \frac{\Delta y(|k - m| - 1/2)}{12\pi^2\sqrt{2k_0}}\Gamma^2(1/4)$$
$$\times \int_{(|j-l|-1/2)\Delta x}^{(|j-l|+1/2)\Delta x}\left[x^2 + \Delta y^2(|k - m| - 1/2)^2\right]^{-5/4} dx \quad (40)$$

In a similar way, for the right-hand side boundary

$$A_{|j-l|,|k-m|}^{(b)} = -\frac{\Delta x(|j - l| + 1/2)}{12\pi^2\sqrt{2k_0}}\Gamma^2(1/4)$$
$$\times \int_{(|k-m|-1/2)\Delta y}^{(|k-m|+1/2)\Delta y}\left[y^2 + \Delta x^2(|j - l| + 1/2)^2\right]^{-5/4} dy \quad (41)$$

and for the left-hand side boundary

$$A_{|j-l|,|k-m|}^{(d)} = \frac{\Delta x(|j - l| - 1/2)}{12\pi^2\sqrt{2k_0}}\Gamma^2(1/4)$$
$$\times \int_{(|k-m|-1/2)\Delta y}^{(|k-m|+1/2)\Delta y}\left[y^2 + \Delta x^2(|j - l|1/2)^2\right]^{-5/4} dy \quad (42)$$
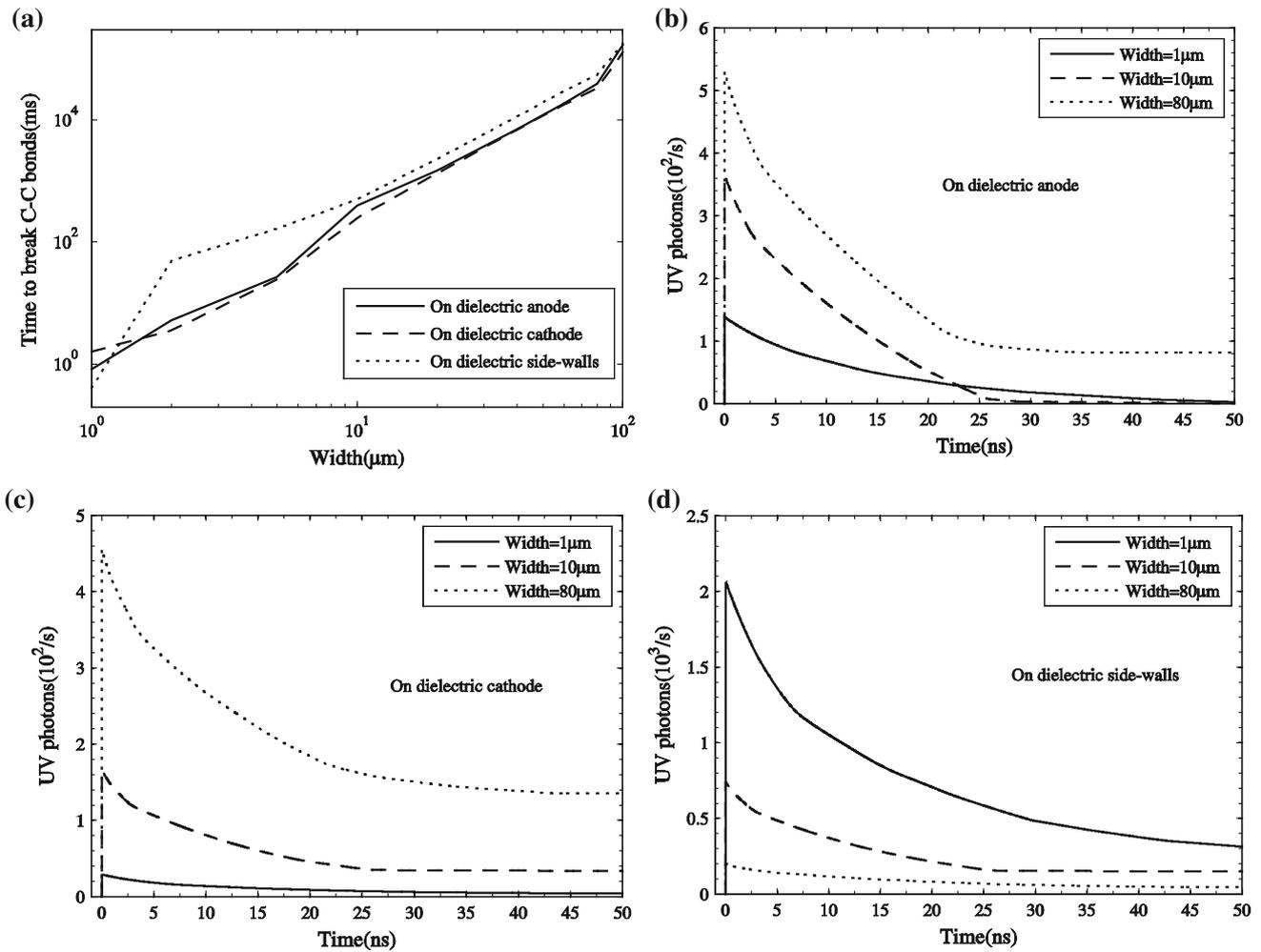
Fig. 18 **a** Time required to break all C–C bonds (t_{cc}) on surrounding dielectrics versus width of narrow channel, and the time history of total amount of UV photons arriving dielectric, **b** anode, **c** cathode, **d** side-walls for three different values of width of the narrow channel

Finally

$$A_{jk;lm} = \delta_{jl}\delta_{km} + A^{(a)}_{|j-l|,|k-m|} + A^{(b)}_{|j-l|,|k-m|}$$
$$+ A^{(c)}_{|j-l|,|k-m|} + A^{(d)}_{|j-l|,|k-m|} \tag{43}$$

Appendix 3: Derivation of spectral radiation flux

At the back plate, spectral photon flux is calculated as;

$$F(r,v) = \frac{1}{4\pi} \int_{V'} \frac{S_r(r')g(v)e^{-k(v)|r-r'|}}{|r-r'|^2} \hat{R} \cdot \hat{n} dV' \tag{44}$$

where $r = (x_i, y_0, 0)$ is a location on the phosphor surface, V' is the volume of the plasma region, and $S_r(\acute{r})$ is the photon emission rate defined as:

$$S_r(r') = n^r(r')/\tau_v \tag{45}$$

With the piecewise constant approximation:

$$F(x_i, v) = \frac{g(v)}{4\pi}$$

$$\sum_{j=1}^{N_x} \sum_{k=1}^{N_y} S_r(x_j, y_k) \int_{x_j-\Delta x/2}^{x_j+\Delta x/2} dx'$$

$$\int_{y_k-\Delta y/2-y_0}^{y_k+\Delta y/2-y_0} dy' \int_{-\infty}^{\infty} dz' y'$$

$$\times \frac{\exp[-k(v)\sqrt{(x_i-x')^2 + y'^2 + z'^2}]}{[(x_i-x')^2 + y'^2 + z'^2]^{3/2}} \tag{46}$$

If we consider three-dimensional distribution of the excited state, the infinite range of z directional integral should be changed to a finite range. However, we assume infinitely long z length with only two-dimensional distribution.

(a)

(b)
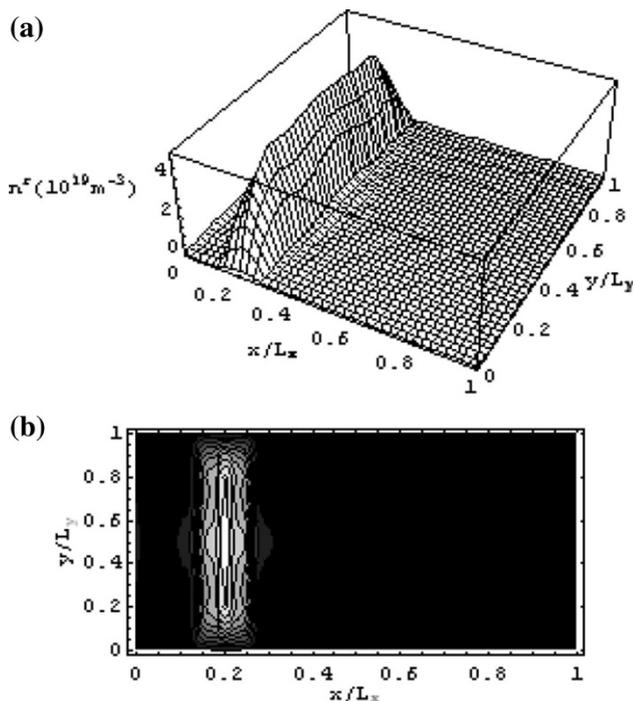
Fig. 19 **a** Surface plot and **b** contour map of radiative states (average respect to time) inside narrow channel; applied field across narrow channel $E = 40$ kV/mm, narrow channel length $L_x = 20$ μm, narrow channel width $L_y = 2$ μm, gas pressure inside narrow channel $P_g = 760$ Torr

(a)

(b)
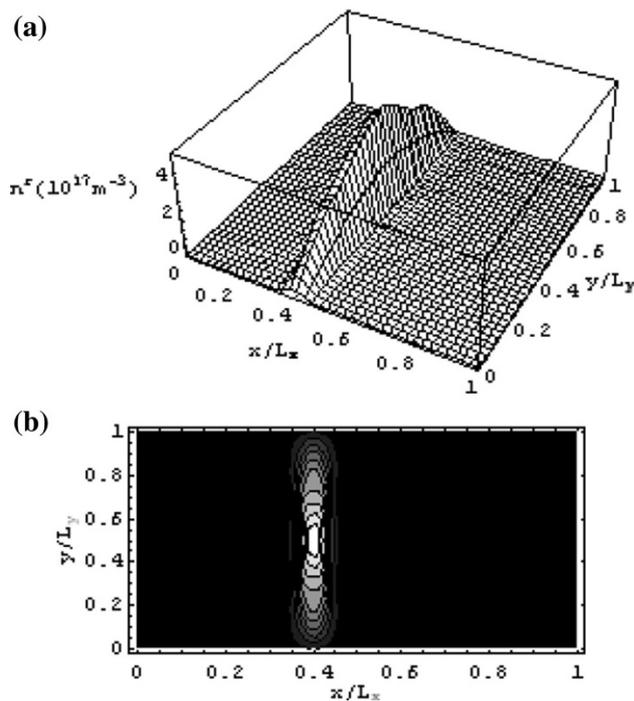
Fig. 20 **a** Surface plot and **b** contour map of radiative states (average respect to time) inside narrow channel; applied field across narrow channel $E = 40$ kV/mm, narrow channel length $L_x = 20$ μm, narrow channel width $L_y = 10$ μm, gas pressure inside narrow channel $P_g = 760$ Torr

With $R_\perp = [(x_i - x')^2 + y'^2]^{1/2}$, $R = R_\perp \sec \theta$ and $z' = R_\perp \tan \theta$,

$$F(x_i, v) = \frac{g(v)}{4\pi} \sum_{j=1}^{N_x} \sum_{k=1}^{N_y} S_r(x_j, y_k) \int_{x_j - \Delta x/2}^{x_j + \Delta x/2} dx'$$

$$\times \int_{y_k - \Delta y/2 - y_0}^{y_k + \Delta y/2 - y_0} \frac{1}{R_\perp^2} dy' \int_0^{\pi/2} \exp[-k(v)R_\perp \sec \theta] \cos \theta \, d\theta \tag{47}$$

With the relation that

$$\int_0^{\pi/2} \cos \theta \exp(-\alpha \sec \theta) d\theta = \int_0^\infty \frac{\exp(-\alpha \cosh z)}{\cosh^2 z} dz = Ki_2(\alpha) \tag{48}$$

$$F(x_i, v) = \frac{g(v)}{4\pi} \sum_{j=1}^{N_x} \sum_{k=1}^{N_y} S_r(x_j, y_k) \int_{x_j - \Delta x/2}^{x_j + \Delta x/2} dx'$$

$$\times \int_{y_k - \Delta y/2 - y_0}^{y_k + \Delta y/2 - y_0} dy' \frac{Ki_2[k(v)\sqrt{(x_i - x')^2 + y'^2}]}{[(x_i - x')^2 + y'^2]} \tag{49}$$

where $Ki_2(x)$ is the second repeated integral of the zeroth-order modified Bessel function, $K_0(x)$ [65]. However, Eq. (49) needs huge computations, and thus we calculate it using average distance between the phosphor surface and

(a)

(b)
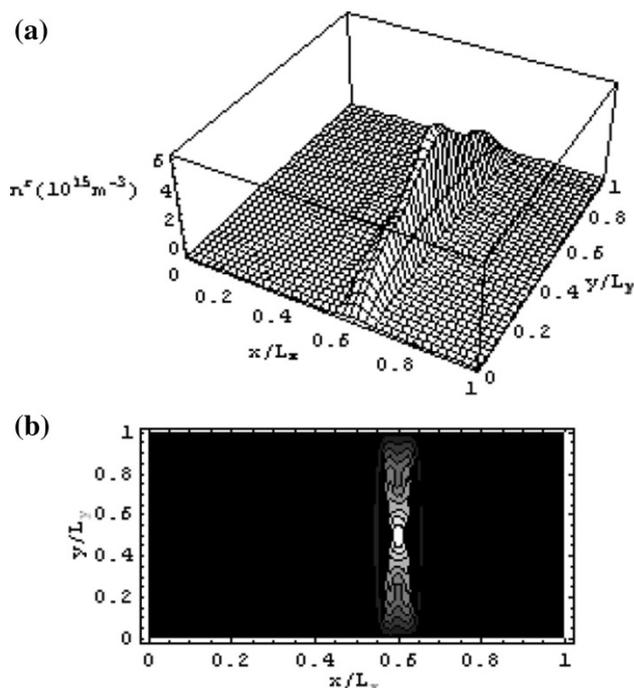
Fig. 21 **a** Surface plot and **b** contour map of radiative states (average respect to time) inside narrow channel; applied field across narrow channel $E = 40$ kV/mm, narrow channel length $L_x = 20$ μm, narrow channel width $L_y = 80$ μm, gas pressure inside narrow channel $P_g = 760$ Torr
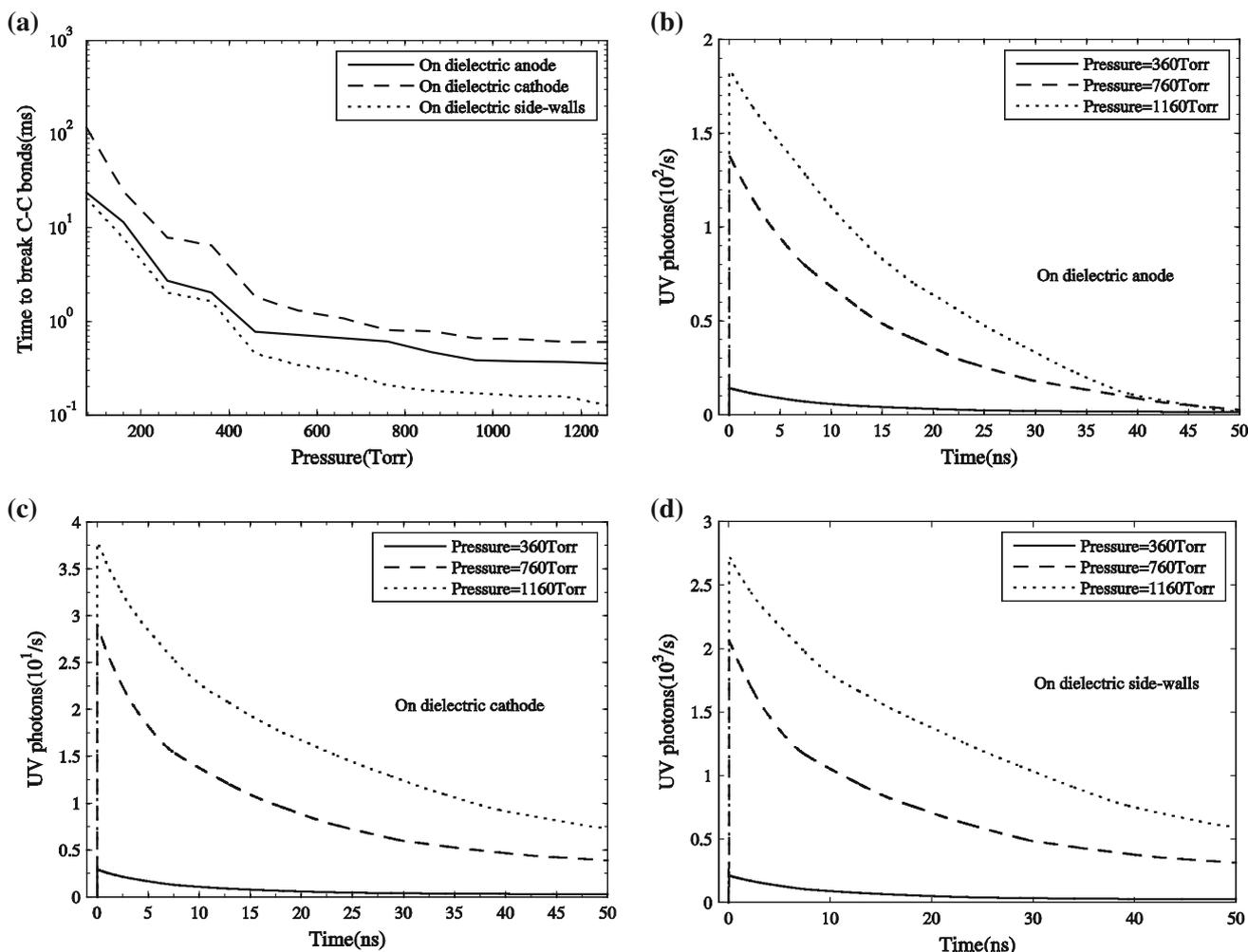
Fig. 22 **a** Time required to break all C–C bonds (t_{cc}) on surrounding dielectrics versus gas pressure inside the narrow, and the time history of total amount of UV photons arriving dielectric, **b** anode, **c** cathode, **d** side-walls for three different values of gas pressure in the narrow channel

the center of the cell where a photon is emitted, which is defined as R_0. If R_0 is enough larger than Δx and Δy, we can pull $R \cdot \hat{n}$ out of the volume integral in Eq. (44), and thus

$$
\begin{aligned}
F(r,v) &= \frac{1}{4\pi} R \cdot \hat{n} \int_{V'} \frac{S_{\mathrm{r}}(r')g(v)\mathrm{e}^{-k(v)|r-r'|}}{|r-r'|^3} \mathrm{d}V' \\
&= -\frac{g(v)}{4\pi} \sum_j \sum_k S_{\mathrm{r}}(x_j, x_k) R_0 \cdot \hat{n} \frac{1}{R_{\perp 0}^2} \\
&\quad \times Ki_2[k(v)R_{\perp 0}]\Delta x \Delta y
\end{aligned}
\tag{50}
$$

$$
\begin{aligned}
F(x_i, v) &= \frac{g(v)}{4\pi} \sum_{j=1}^{N_x} \sum_{k=1}^{N_y} S_{\mathrm{r}}(x_j, y_k)(y_k - y_0) \\
&\quad \times \frac{Ki_2\left[k(v)\sqrt{(x_j - x_i)^2 + (y_k - y_0)^2}\right]}{(x_j - x_i)^2 + (y_k - y_0)^2} \Delta x \Delta y
\end{aligned}
\tag{51}
$$

$$
= \sum_{j=1}^{N_x} \sum_{k=1}^{N_y} n_{jk}^{\mathrm{r}} \tilde{F}_{|i-j|,k}^{v}
\tag{52}
$$

where

$$
\begin{aligned}
\tilde{F}_{|i-j|,k}^{v} &= \frac{g(v)}{4\pi\tau_v} \Delta x \Delta y \\
&\quad \times \frac{Ki_2\left[k(v)\sqrt{(x_j - x_i)^2 + (y_k - y_0)^2}\right]}{(x_j - x_i)^2 + (y_k - y_0)^2}
\end{aligned}
\tag{53}
$$

Appendix 4: Derivation of total radiation flux

The total photon flux is:

$$
F(r) = \int_0^\infty F(r,v)\mathrm{d}v
\tag{54}
$$

(a)

(b)
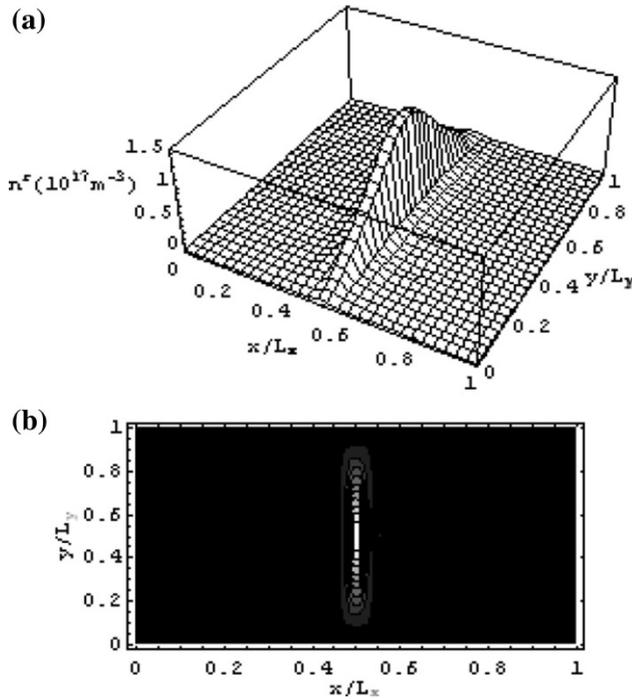
Fig. 23 **a** Surface plot and **b** contour map of radiative states (average respect to time) inside narrow channel; applied field across narrow channel $E = 40$ kV/mm, narrow channel length $L_x = 20$ μm, narrow channel width $L_y = 1$ μm, gas pressure inside narrow channel $P_g = 76$ Torr

(a)

(b)

Fig. 24 **a** Surface plot and **b** contour map of radiative states (average respect to time) inside narrow; applied field across narrow channel $E = 40$ kV/mm, narrow channel length $L_x = 20$ μm, narrow channel width $L_y = 1$ μm, gas pressure inside narrow channel $P_g = 360$ Torr

(a)

(b)

Fig. 25 **a** Surface plot and **b** contour map of radiative states (average respect to time) inside narrow channel; applied field across channel $E = 40$ kV/mm, channel length $L_x = 20$ μm, channel width $L_y = 1$ - μm, gas pressure inside channel $P_g = 1,160$ Torr
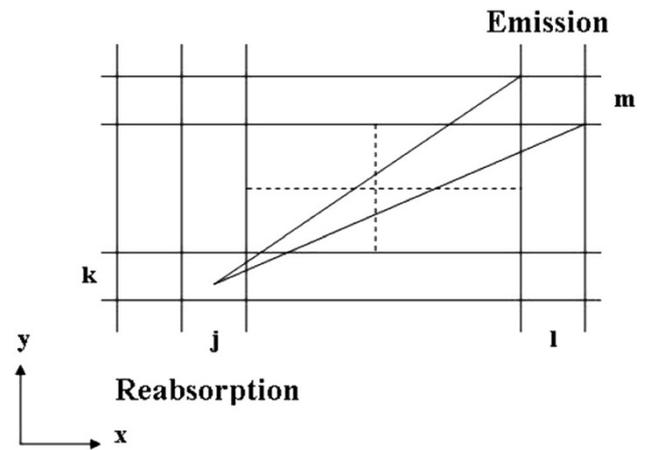
Fig. 26 Simulation mesh diagram of radiation transport for a photon emitted at (l, m)th cell to be reabsorbed at the (j, k)th cell. With the piecewise-constant approximation, the density at each cell is assumed to be constant [39]

From the integral of Eq. (46) over frequency v:

$$F(r, v) = \frac{1}{4\pi} \int_{V'} \frac{S_r(r') T(|r - r'|)}{|r - r'|^2} \hat{R} \cdot \hat{n} dV' \tag{55}$$

With a high opacity approximation, $T(R) = (\pi k_0 R)^{-1/2}$:

$$F(x_i) = \frac{1}{4\pi\sqrt{\pi k_0}} \int_{V'} \frac{S_r(r')}{|r-r'|^{7/2}} R \cdot \hat{n} dV'$$

$$\frac{1}{4\pi\sqrt{\pi k_0}} \sum_{j=1}^{N_x} \sum_{k=1}^{N_y} S_r(x_j, y_k) \int_{x_j-\Delta x/2}^{x_j+\Delta x/2} dx'$$

$$\times \int_{y_k-\Delta y/2-y_0}^{y_k+\Delta y/2-y_0} dy' \int_{-\infty}^{\infty} dz' y' \times \left[(x_i-x')^2 + y'^2 + z'^2\right]^{-7/4}$$

$$(56)$$

$$F(x_i) = \frac{\Gamma^2(1/4)}{6\pi^2\sqrt{2k_0}} \sum_{j=1}^{N_x} \sum_{k=1}^{N_y} S_r(x_j, y_k)$$

$$\times \int_{x_j-\Delta x/2}^{x_j+\Delta x/2} \left\{ \left[(x_i-x')^2 + (y_k - \Delta y/2 - y)^2\right]^{-7/4} \right.$$

$$\left. - \left[(x_i-x')^2 + (y_k + \Delta y/2 - y)^2\right]^{-7/4} \right\} dx'$$

$$(57)$$

$$= \sum_{j=1}^{N_x} \sum_{k=1}^{N_y} n_{jk}^r F_{|i-j|,k}$$

$$(58)$$

where

$$F_{|i-j|,k} = \frac{\Gamma^2(1/4)}{6\pi^2\tau_v\sqrt{2k_0}}$$

$$\times \int_0^{\Delta x/2} \left\{ \left[(|x_i-x_j|+x')^2 + (y_k-y_0)^2\right]^{-1/4} \right.$$

$$+ \left[(|x_i-x_j|-x')^2 + (y_k-y_0)^2\right]^{-1/4} - \left[(|x_i-x_j|+x')^2 \right.$$

$$+ (y_k-y_0+\Delta y)^2\right]^{-1/4} - \left[(|x_i-x_j|-x')^2 \right.$$

$$\left. + (y_k-y_0+\Delta y)^2\right]^{-1/4} \right\} dx$$

$$(59)$$

References

1. Seralathan, K.E., Mahajan, A., Gupta, N.: Modelling of electric tree progression due to space charge modified fields. J. Phys. D Appl. Phys. **41**(3), 105501-1–105501-9 (2008)
2. Singh, B., Sharma, N.: Mechanistic implications of plastic degradation. Polym. Degrad. Stab. **93**, 561–584 (2008)
3. Laurent, C., Mayoux, C.: Analysis of the propagation of electrical treeing using optical and electrical methods. IEEE TEI **EI-15**(1), 33–42 (1980)
4. Laurent, C., Mayoux, C.: Light detection during the initiation of electrical treeing at room temperature. J. Phys. D Appl. Phys. **14**, 1903–1910 (1981)
5. Laurent, C., Mayoux, C., Noel, S., Sinisuka, N.I.: A study of emission lines from electrical trees. IEEE TEI **EI-18**(2), 125–130 (1983)
6. Champion, J.V., Dodd, S.J., Stevens, G.C.: Quantitative measurement of light emission during the early stages of electrical breakdown in epoxy and unsaturated polyester resins. J. Phys. D Appl. Phys. **26**, 819–828 (1993)
7. Champion, J.V., Dodd, S.J., Stevens, G.C.: Long-term light emission measurement and imaging during the early stages of electrical breakdown in epoxy resin. J. Phys. D Appl. Phys. **27**, 604–610 (1994)
8. Champion, J.V., Dodd, S.J., Alison, J.M.: The correlation between the partial discharge behaviour and the spatial and temporal development of electrical trees grown in an epoxy resin. J. Phys. D Appl. Phys. **29**, 2689–2695 (1996)
9. Champion, J.V., Dodd, S.J., Zhao, Y., Vaughan, A.S., Brown, M., Davies, A.E.: Morphology and the growth of electrical trees in a propylene/ethylene copolymer. IEEE TDEI **8**(2), 284–292 (2001)
10. Kaneiwa, H., Suzuoki, Y., Mizutani, T.: Partial discharge characteristics and tree inception in artificial simulated tree channels. IEEE TDEI **7**(6), 843–848 (2000)
11. Kaneiwa, H., Suzuoki, Y., Mizutani, T.: Characteristics of partial discharges artificial simulated tree channels during in tree propagation. IEEE TDEI **8**(1), 72–77 (2001)
12. Wu, K., Suzuoki, Y., Mizutani, T., Xie, H.: A novel physical model for partial discharge in narrow channels. IEEE TDEI **6**(2), 181–190 (1999)
13. Wu, K., Suzuoki, Y., Mizutani, T., Xie, H.: Model for partial discharges associated with treeing breakdown: I. PDs in tree channels. J. Phys. D Appl. Phys. **33**, 1197–1201 (2000)
14. Wu, K., Suzuoki, Y., Mizutani, T., Xie, H.: Model for partial discharges associated with treeing breakdown: II. Tree growth affected by PDs. J. Phys. D Appl. Phys. **33**, 1202–1208 (2000)
15. Wu, K., Suzuoki, Y., Mizutani, T., Xie, H.: Model for partial discharges associated with treeing breakdown: III. PD extinction and re-growth of tree. J. Phys. D Appl. Phys. **33**, 1209–1218 (2000)
16. Nagano, M., Kobayakawa, K., Sakaki, N., Ando, K.: Photon yields from nitrogen gas and dry air excited by electrons. Astropart. Phys. **20**, 293–309 (2003)
17. Encyclopedia of polymer science and technology. In: Radiation Chemistry of Polymers. Wiley, New York (2005)
18. Dissado, L.A., Fothergill, J.C.: Electrical Degradation and Breakdown in Polymers. Peter Perigrinus, London (1992)
19. Hwang, Y.J.: Characterization of atmospheric pressure plasma interactions with textile/polymer substrates. Ph. D thesis, North Carolina State University, USA (2003)
20. Ganjovi, A.A., Gupta, N., Raju, G.R.G.: A kinetic model of a PD pulse within voids of sub-millimeter dimensions. IEEE TDEI **16**(6), 1743–1754 (2009)
21. Vahedi, V., DiPeso, G.: Simultaneous potential and circuit solution for two-dimensional bounded plasma simulation codes. J. Comput. Phys. **131**, 149–163 (1997)
22. Vahedi, V., Birdsall, C.K., Lieberman, M.A., DiPeso, G., Rognlien, T.D.: Verification of frequency scaling laws for capacitive radio-frequency discharges using two-dimensional simulations. Phys. Fluids B **5**, 2719–2729 (1993)
23. Lawson, W.S.: Particle simulation of bounded 1D plasma systems. J. Comput. Phys. **80**, 253–276 (1989)
24. Ganjovi, A.: Effect of electric field on PD activity and damage into solid dielectric materials. Int. J. Math. Model. Comput. (IJM2C) (2014, in press)
25. Ganjovi, A.: A parametric study of evaluation of damage into solid dielectrics due to PD activity using a kinetic model. Majlesi J. Electr. Eng. (MJEE) (accepted)
26. Holstein, T.: Imprisonment of resonance radiation in gases. Phys. Rev. **72**(12), 1212–1233 (1947)
27. Holstein, T.: Imprisonment of resonance radiation in gases. II. Phys. Rev. **83**(6), 1159–1168 (1951)
28. Hagelaar, G.J.M., Klein, M.H., Snijkers, R.J.M.M., Kroesen, G.M.W.: Resonance radiation transport in plasma display panels. J. Appl. Phys. **88**(10), 5442–5538 (2000)
29. Straaten, T., Kushner, M.J.: A Monte-Carlo model of xenon resonance radiation transport in a plasma display panel cell:

transition from optically thick to thin regimes. J. Appl. Phys. **87**(6), 2700–2707 (2000)

30. Molisch, A.F., Oehry, B.P., Schupita, W., Magerl, G.: McTrap, a program for the computation of radiation trapping in 3-level atoms including bleaching effects. Comput. Phys. Commun. **93**, 127–135 (1996)

31. Molisch, A.F., Oehry, B.P., Schupita, W., Magerl, G.: Radiation-trapping in cylindrical and spherical geometries. J. Qum. Spec-msc. Rdal. Tratufer **49**(4), 361–370 (1993)

32. Molisch, A.F., Oehry, B.P., Schupita, W., Magerl, G.: RAD-TRAP 2, a program for the solution of the Holstein equation of radiation trapping. Comput. Phys. Commun. **77**, 255–262 (1993)

33. Molisch, A.F., Oehry, B.P., Schupita, W., Magerl, G.: Radiation-trapping in cylindrical and spherical geometries. J. Qum. Spec-msc. Rdal. Tratufer **48**(4), 377–396 (1992)

34. Lawler, E., Parker, G.J., Hitchon, W.N.G.: Radiation trapping simulations using propagator function method. J. Quant. Spec-trosc. Radiat. Transf. **49**(6), 627–638 (1993)

35. Sahni, O., Lanza, C., Howard, W.E.: One-dimensional numerical simulation of AC discharges in a high-pressure mixture of Ne + 0.1 % Ar confined to a narrow gap between insulated metal electrodes. J. Appl. Phys. **49**, 2365–2375 (1978)

36. Lee, H.J., Verboncoeur, J.P.: Simulation of a positive column discharge with a one-dimensional radial radiation transport coupled particle-in-cell model. J. Appl. Phys. **90**(10), 4957–4965 (2001)

37. Lee, H.J., Verboncoeur, J.P.: A radiation transport coupled particle-in-cell simulation: I. Description of the model. Phys. Plasmas **8**(6), 3077–3088 (2001)

38. Lee, H.J., Verboncoeur, J.P.: A radiation transport coupled particle-in-cell simulation II. Simulation results in a one-dimensional planar model. Phys. Plasmas **8**, 3089–3095 (2001)

39. Lee, H.J., Kim, H.C., Yang, S.S., Lee, J.K.: Two-dimensional self-consistent radiation transport model for plasma display panels. J. Appl. Phys. **9**(6), 2822–2830 (2002)

40. Birdsall, C.K.: Particle-in-cell charged-particle simulations, plus Monte Carlo collisions with neutral atoms, PIC-MCC. IEEE Trans. Plasma Sci. **19**, 65–85 (1995)

41. Vahedi, V., Surendra, M.: Monte-Carlo collision model for particle-in-cell method: application to argon and oxygen discharges. Comput. Phys. Commun. **87**, 179–198 (1995)

42. Birdsall, C.K., Langdon, A.B.: Plasma Physics Via Computer Simulation. McGraw-Hill, New York (1985)

43. Roldan, A., Perez, J.M., Williart, A., Blanco, F., Garcia, G.: Energy deposition model for low-energy electrons (10–10 000 eV) in air. J. Appl. Phys. **95**(10), 5865–5870 (2004)

44. Zhang, W., Fisher, T.S., Garimella, S.V.: Simulation of ion generation and breakdown in atmospheric air. J. Appl. Phys. **96**, 6066–6072 (2004)

45. Mardahl, P.J., Cartwright, K.L.: Reducing numerical heating in 1-D PIC simulations. In: Annual Progress Report for 1993, Plasma Theory and Simulation Group, University of California Technical Memorandum, Electronics Research Laboratory, Berkeley (1993)

46. Mardahl, P.J., Verboncoeur, J.P.: Charge conservation in electromagnetic PIC codes; spectral comparison of Boris/DADI and Langdon-Marder methods. Comput. Phys. Commun. **106**, 219–229 (1997)

47. Verboncoeur, J.P.: Symmetric spline weighting for charge and current density in particle simulation. J. Comput. Phys. **174**, 421–427 (1997)

48. Kennedy, J.T., Wetzer, J.M.: Numerical study of the avalanche to streamer transition in N_2 and dry air. In: Christophorou, L.G., Oltoff, J.K. (eds.) Gaseous Dielectrics. Plenum press, New York (1994)

49. Arqueros, F., Blanco, F., Castellanos, A., Ortiz, M., Rosado, J.: The yield of air fluorescence induced by electrons. Astropart. Phys. **26**, 231–242 (2006)

50. Bennett, W.R., Flint, J.: $Ar(^3P_2)$-$N_2(C^3\prod_u)$ excitation transfer cross section and radiative lifetimes of the nitrogen molecular laser transitions. Phys. Rev. A **18**(6), 2527–2532 (1978)

51. Hatamoto, T., Okunishi, M., Matsumoto, M., Lischke, T., Shimada, K., Pruemper, G., Kong, F., Ueda, K., Dissociative ionization of methanol in moderate intense laser fields. Chem. Phys. Lett **434**, 205–209 (2007)

52. Theodorou, D.N.: Understanding and predicting structure property relations in polymeric materials through molecular simulations. Mol. Phys. **102**, 147–166 (2004)

53. Bartnikas, R.: Some observations on the character of corona discharges in short gap spaces. IEEE TEI **6**(2), 63–75 (1971)

54. Bartnikas, R., Levi, J.H.E.: A simple pulse-height analyzer for partial discharge-rate measurements. IEEE Trans Instrum Meas **IM-18**, 341–345 (1969)

55. Bartnikas, R.: Engineering dielectrics, vol. 1. In: Bartnikas, R., McMahon, E.I. (eds.) Corona Measurement and Interpretation, SlT669. ASTM, Philadelphia (1979)

56. Bartnikas, R.: Discharge rate and energy loss in helium at low frequencies. Electr. Eng. **52**, 348–359 (1969)

57. Bartnikas, R., Levi, J.: Improved pulsed discharge rate measuring apparatus for ionization discharge studies at low frequencies. Rev. Sci. Instrum. **37**, 1245–1251 (1966)

58. Gaxiola, E.H.R., Wetzer, J.M.: Partial discharges in micrometer voids PTFE, pp. 16–19. IEEE International Symposium on Electrical Insulation, Montreal (1996)

59. Tanaka, T., Ikeda, Y.: Internal discharges in polyethylene with an artificial cavity. IEEE TPAS **PAS-90**(6), 2692–2702 (1971)

60. Mayoux, C., Laurent, C.: Contribution of partial discharges to electrical breakdown of solid insulating materials. IEEE TDEI **2**(4), 641–652 (1995)

61. Champion, J.V., Dodd, S.J.: An approach to the modeling of partial discharges in electrical trees. J. Phys. D Appl. Phys. **31**, 2305–2314 (1998)

62. Champion, J.V., Dodd, S.J.: Simulation of partial discharges in conducting and non-conducting electrical tree structures. J. Phys. D Appl. Phys. **34**, 1235–1242 (2001)

63. Noskov, M.D., Malinovski, A.S., Sack, M., Schwab, A.J.: Self-consistent modeling of electrical tree propagation and PD activity. IEEE TDEI **7**(6), 725–733 (2000)

64. Gu, W.Y., Laurent, C., Mayoux, C.: Characteristics of discharges inside simulated tree channels under impulse voltage. J. Phys. D Appl. Phys. **19**, 2197–2207 (1986)

65. Abramowitz, M., Stegun, I.A.: Handbook of Mathematical Functions, p. 483. Dover, New York (1965)